RESEARCH ARTICLE

Explicitly Reconstructing RAMI-V Scenes for Accurate 3-Dimensional Radiative Transfer Simulation Using the LESS Model

Kun Zhou[1], Donghui Xie[1*], Jianbo Qi[2], Zhixiang Zhang[1], Xinyu Bo[1], Guangjian Yan[1], and Xihan Mu[1]

[1]State Key Laboratory of Remote Sensing Science, Faculty of Geographical Science, Beijing Normal University, Beijing 100875, China. [2]State Forestry and Grassland Administration Key Laboratory of Forest Resources and Environmental Management, Beijing Forestry University, Beijing 100083, China.

*Address correspondence to: xiedonghui@bnu.edu.cn

Radiative transfer (RT) simulation based on reconstructed 3-dimensional (3D) vegetation scenarios can promote the validation and development of various retrieval algorithms to monitor the growing states of vegetation in large-scale, multi-angular, and multi-sensor ways. The radiation transfer model intercomparison (RAMI) has made great contributions to providing abstract and actual 3D vegetation scenarios, and to the benchmarking of RT models under developed evaluation systems. To date, RAMI has been updated to the fifth phase (RAMI-V). In this study, we try to implement explicit conversion from all the RAMI-V scenes to generic structural models in the Wavefront OBJ format. These reconstructed scenes are applied in the LESS RT model to probe the ability of its RT solvers to simulate all sorts of remote sensing observations and radiative budget, including the bidirectional reflectance factor (BRF), albedo, fraction of photosynthetically active radiation absorbed by vegetation, and threshold hemispherical photograph (THP). BRF simulations fully explain angle effects as well as variation and robustness of the normalized difference vegetation index. Energy conservation is well validated between simulated absorption and albedo. The gap fraction derived from THP is analyzed in directional and total situations. In addition, this paper guides us how to simplify basic geometries and tune the illumination resolution (0.02 is optimal) to balance the simulation accuracy and efficiency. The generic structural models and reliable simulation results can be referenced by other RT models and retrieval algorithms.

Introduction

Radiative transfer (RT) models are useful to quantify the spreading mechanism of electromagnetic radiation by describing interactions between electromagnetic radiation and vegetation canopies [1]. They play an essential role in the interpretation of remote sensing (RS) observations [2], which has promoted the validation and development of various retrieval algorithms for key bio-geophysical properties of vegetation [3–5]. In addition, RT models are capable of guiding field experiments [6,7] and the design of remote sensors [8].

The primitively proposed 1-dimensional (1D) RT models (e.g., SAIL [9]) feature a few parameters and low computational cost. They simplify vegetation canopies as one or multiple horizontal homogeneous layers (e.g., grasses), which cannot accurately represent spatial heterogeneity of canopies. Therefore, geometric–optical (GO) models [10,11] were introduced to describe heterogeneity among the discrete crowns and clumping effects at various scales. Due to the assumption of single regular crown shape, it is difficult for GO models to consider structural differences between the crowns of mixed species (e.g., agro-forestry

scenarios [12]). In order to break through the restrictions of 1D RT models and GO models, 3-dimensional (3D) RT models were proposed with the computational performance gradually improved. Most 3D RT models are mainly developed based on radiosity (e.g., RGM [13] and RAPID [14]) or ray tracing (e.g., DART-Lux [15] and LESS [1]) methods. The path tracing technology is commonly used in those RT models based on ray tracing methods. Some path tracing modes, including the forward path tracing (FPT) mode, the backward path tracing (BPT) mode, and the bidirectional path tracing (BDPT) mode, are selected to satisfy different simulation demands. The FPT mode, which is applied in Rayspread [16] and FLiES [17], produces light paths from the light source to the sensor. For accurate directional bidirectional reflectance factor (BRF) simulations, the photon spread method [18] is proposed by adding light paths contributing to particular view directions, and introduced by Rayspread later with a secondary ray mechanism. However, the FPT mode is not suitable for image simulations due to quantities of invalid light paths. Depending on reversibility of light paths, the BPT mode is used by DIRSIG [19] and VBRT [20] to simulate images more efficiently by producing paths from the

sensor to the light source. In order to deal with simulations of all kinds of RS signals, LESS considers both FPT and BPT modes. In addition to FPT and BPT modes, the BDPT mode is adopted by DART-Lux to improve simulation efficiency compared to standard DART, which employs the discrete ordinates method. The BDPT mode strengthens the connection between the light source and the sensor by linking the vertices of FPT paths to the vertices of BPT paths. The 3D RT models can take more detailed canopies into account with fewer assumptions. Thus, they are frequently used to produce datasets as a standard for validating other models [3,12,21] or retrieval algorithms of RS products [22–24].

Although there are so many advantages, a common challenge for all the 3D RT models is to digitalize those real scenes into the virtual world, especially for vegetation scenes. Most vegetation structures are varied and complex. It is very convenient to create fine but virtual plant models using L-systems [25] and other procedural generation software. Meanwhile, this method requires prior plant knowledge to control the generation of vivid plants. Another explicit tree modeling method reconstructs detailed architecture of wood and foliage from images [26] or terrestrial LiDAR (Light Detection And Ranging) point clouds [27]. Nevertheless, high-quality plant models are difficult to be directly used to build large-scale scenarios due to the heavy memory burden. The turbid medium method implicitly describes canopy structure in the form of voxels [28] or geometric primitives [29,30] with limited structural and radiometric properties. Combined with airborne LiDAR point clouds, the turbid medium method can be easily extended to larger scales [28]. Although the turbid medium method demands fewer computing resources, its RT accuracy cannot maintain good consistency with the explicit methods with respect to complex actual vegetation scenarios [31]. For the explicit modeling methods, the Wavefront OBJ (https://www.fileformat.info/format/wavefrontobj/egff.htm) is a popular plain text format, which can unambiguously describe the geometric structure with several groups of vertices and faces. Therefore, the OBJ format is commonly supported by many 3D RT models.

To approximate structural realism, whether explicit or implicit modeling methods, they are inseparable from field measurements (e.g., LiDAR point clouds, spectra, tree positions, tree species, etc.), whereas field experiments are generally time-consuming and labor-intensive. Since the end of the last century, the radiation transfer model intercomparison (RAMI) exercises have been devoted to comparing and assessing all kinds of RT models, from the first to the fifth phase, under the same well-controlled circumstances. To be compatible with different RT models, RAMI phases provide both simple abstract canopies [2,32–34] and complex actual plant stands [35]. Using these available scenarios, which constitute abundant and precious datasets (including structure, spectra, and reference simulations), can greatly relieve experimental pressures. Hence, in recent decades, RAMI scenes and reference data have been used in many studies [36–42].

In fact, with regard to using RAMI scenes, the structural transformation becomes a stumbling block for the following reasons. First, the structure of RAMI scenes is abstractly described as specific shapes. The formats of these shapes are very clearly defined, but the ways to parse them are customized. Since various RT models employ different methods to build scenes, these shapes will be processed or simplified in different ways, which gives rise to structural discrepancies and, more

seriously, yields deviations of simulations [33,43]. For example, the disc-shape leaves can be replaced by any-sided regular polygons in the explicit methods, while in the implicit methods, they can be described as a group of statistical parameters, such as the foliage area volume density and leaf angle distribution. Second, the coordinate systems and structural definitions of the individual tree components in each scene are slightly different. The origin of the RAMI coordinate system can be located at the center or left lower corner. As for structural definitions, the shape of a branch can be defined as triangular facets or connected cylinders. These differences among the scenes make it difficult to batch transformation via programs. Third, as the structure of the tree models becomes more and more complex, the storage size increases the computational burden of simulations. For instance, a simple shoot is composed of hundreds of needles, which leads to huge memory usage when loading an entire coniferous tree.

With the advent of RAMI-V, the complexity and realism of the scenes have further increased, while more measurements have been asked for. The objective of this paper is to probe the performance of the LESS model (http://lessrt.org/), a newly proposed and well-validated 3D RT model, in simulating various RS observations and radiative budget in the RAMI-V framework, which we have achieved by finishing the following:

- Transforming the structural definitions of all the RAMI-V scenes into the same specific coordinate system in the standard and general Wavefront OBJ format;
- Simulating most of the measurements demanded by RAMI-V and completing their analysis; and
- Quantifying the influence of the structural simplification and illumination resolution on simulations.

Materials and Methods

Components of RAMI-V scenes
Extended from the fourth phase of RAMI (RAMI-IV), the scenes provided by RAMI-V are also divided into 2 types, with 30 abstract and 8 actual canopies in total. The former consists of 14 homogeneous and 16 heterogeneous scenes, while the latter are all heterogeneous.

Canopy structure
As shown in Table S1, the abstract scenes in Groups (a) to (d) are simply filled with disc-like leaves. They accumulated through the past RAMI phases. Even though the actual scenes in Group (e) have a realistic look, they are still virtual, per se, because the individual trees composing them were constructed by procedural generation software (e.g., xfrog [44] and arbaro [45]) on the basis of in situ inventory data. The 2 scenes in Group (f) were newly proposed in RAMI-V. HET50 [46] described the architecture of broad-leaved overstory and grassy understory in detail, and the stands within it were virtually generated by OnyxTREE (www.onyxtree.com). Different from previously published scenarios, HET51 [27] became the first one that directly used the terrestrial LiDAR point clouds to reconstruct all the trees with the help of the TreeQSM [47] and FaNNI [48] algorithms, which, to some extent, was also structurally closest to reality.

Although LESS provides both explicit (facet) and implicit (turbid medium) modeling methods, the explicit canopy

structure in the Wavefront OBJ format was used to maintain the simulation accuracy with fewer assumptions. Both abstract and actual scenes are made up of many basic geometries, including triangles, discs, cylinders, ellipsoids, and circular truncated cones. In order to adapt to computers, some geometries have to be simplified. As illustrated in Fig. 1A, the disc, cylinder and circular truncated cone are replaced with a regular octagon, hexagonal prism, and hexagonal prismoid, whereas the ellipsoid is split into 2 hexagonal pyramids. It is notable that the surface area of all the simplified geometries is the same as that of the original geometries to keep the projected area basically unchanged [49]. As a result, their scale is unavoidably enlarged. Specifically, the cylinder and circular truncated cone consist of a lateral face and 2 base faces, but we only maintain

the lateral area unchanged because the lateral face is more important than the base face for intercepting the sunlight.

The structure of an entire scene hinges both on the components (e.g., leaf/shoot, stem, branch, twig, etc.) and on the positions of the individual trees. It can be reconstructed through 3 stages of replication (Fig. 1). At the first stage, 3D transformation, including rotation, translation, and scaling, is applied to the simplified basic geometries, and then we can obtain various individual tree components (Fig. 1B), among which shoots and leaves are 2 kinds of foliage representation corresponding to coniferous and broad-leaved trees. The goal of the next stage is to generate the full foliage of a tree using a shoot or leaf as a template. Unlike the basic geometries, the foliage templates are limited to being transformed rigidly due to the
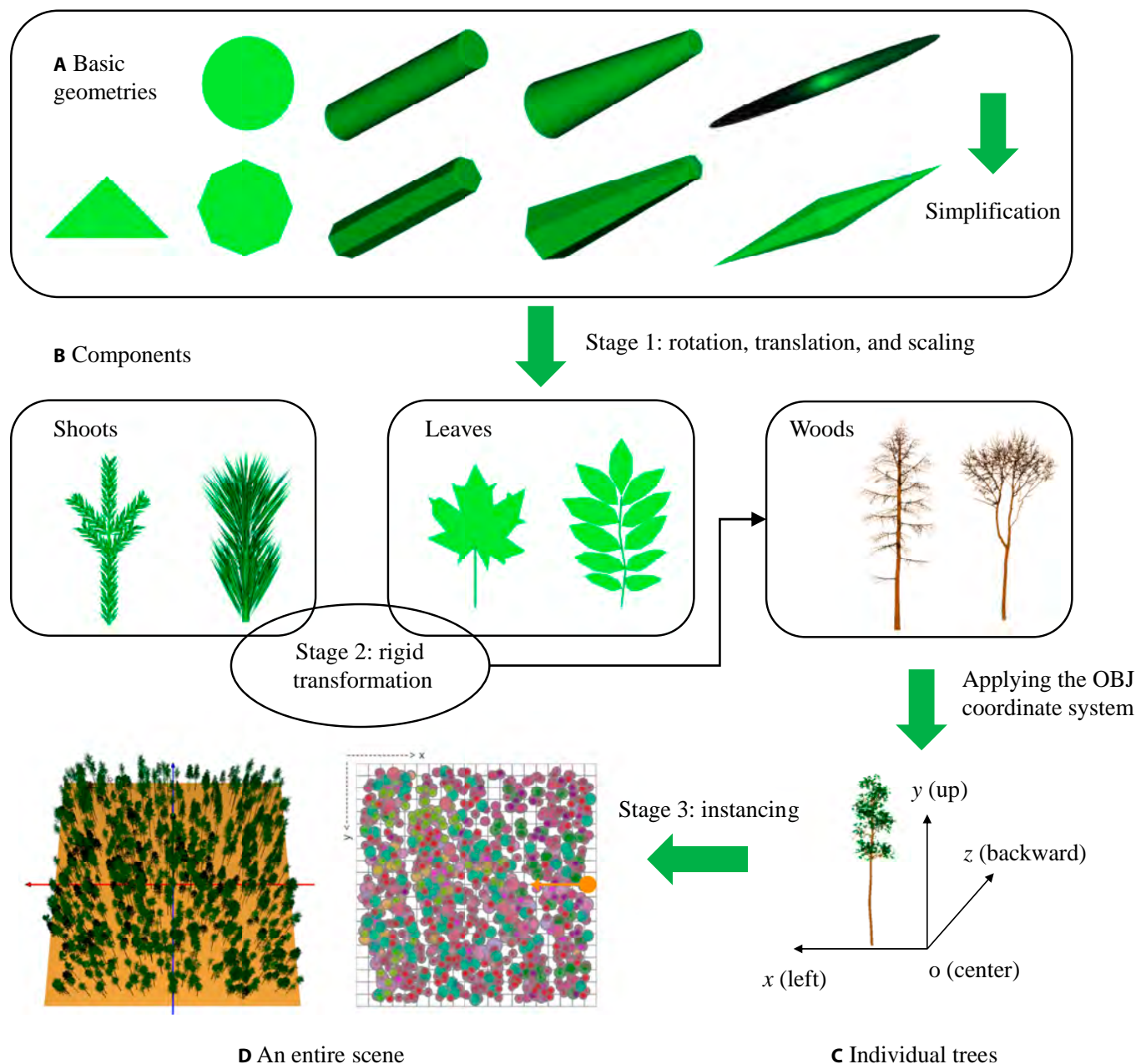
Fig. 1. The 3 stages of replication implementing reconstruction from (A) basic geometries to (D) an entire scene. The OBJ models in (A), (B), and (C) were visualized using CloudCompare (http://www.cloudcompare.org/). The entire scene in (D), including 3D viewing and 2D distribution with individual tress (circles in different colors), was displayed in LESS.

allometry. Before the last stage, individual trees (Fig. 1C) should be located in the OBJ coordinate system, which was adopted by the model coordinate system (MCS) of LESS. It is convenient to transform the MCS of RAMI into the OBJ coordinate system because both are right-handed systems. The "instance" technique utilized by LESS is able to copy all kinds of individual trees to the planting coordinate system (PCS) of LESS in a way, which supports rotation of 1 degree of freedom (DOF) and translation of 3 DOFs. Rather than load all the trees at one time, the "instance" technique can greatly lighten burden on storage and computation. Although the right-handed PCS of RAMI-V has 2 forms, with the origin at the center or lower left corner, according to the detailed information of each scene provided by the RAMI website, it is not hard to unify them to the left-handed PCS of LESS. By the way, the LESS GUI greatly helps in checking if the 2-dimensional (2D) distribution (Fig. 1D) of the individual trees corresponded to that displayed on the RAMI website.

Spectral characteristics
Various architectural components of vegetation scenes are bound to different spectral characteristics (e.g., reflectance and transmittance; Fig. 2). The transmittance of background and woody elements were defaulted to be zero. For those components that featured Lambertian scattering properties, 2 faces had the same single reflectance. The semi-empirical RPV model [50] was introduced to represent the directional reflectance characteristics of different types of backgrounds, such as Group (b) in Table S1. There were 13 spectral bands from the visible to near-infrared (NIR) spectral domains selected to cover the bands designed for the 3 satellite instruments: Sentinel-3 OLCI, Terra MODIS, and Sentinel-2 MSI. The bands O03 (433.6 to 452.3 nm), O06 (551 to 569.8 nm), O08 (655.9 to 674.6 nm), and O17 (851.2 to 880 nm) composed the intersection set of bands from these instruments. Naturally, they were chosen to serve as the blue, green, red, and NIR bands, respectively.

Illumination and observation
Two illumination conditions were adopted by RAMI-V in order to satisfy different measurements. One of them is direct light,
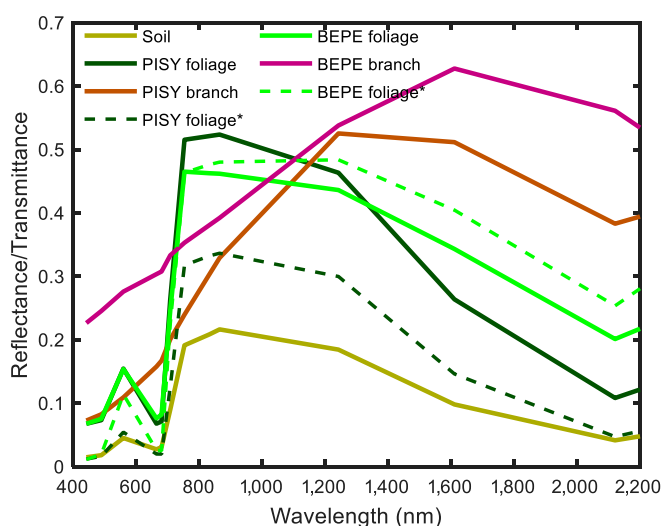
which emulates clear days and depends on the specific sun geometry in the form of the sun azimuth angle (SAA) and sun zenith angle (SZA). For most measurements, all the abstract scenes share 21 sun geometries, while the sun geometries of the actual scenes differ in number and angle. Another illumination condition is diffuse light, which emulates cloudy days, and in LESS, it can be controlled by a group of proportions where a proportion of 1 means white sky, and 0 means black sky. The measurements defined by RAMI-V require various observation sensors and geometries formed by the view azimuth angle (VAA) and view zenith angle (VZA) to be as similar to the actual RS observations as possible. Take BRF as an example, the BRFs in the principle plane and orthogonal plane are sampled at 2° VZA intervals. Specifically, as a new measurement, satellite BRFs follow the observation time of the different satellite instruments, when both the sun and view geometries change synchronously.

Other RAMI scenes
Since the reference data of RAMI-V exercise have not been released, the past RAMI phases were also used to implement validation in the Validation with ROMC and Rayspread section. An abstract scene HET01_DIS_UNI and an actual scene HET07_JPS_SUM (Table 1) were respectively selected from RAMI-3 and RAMI-IV. The structural definitions of these 2 representative scenes are the same as those given by RAMI-V. Therefore, we employed the same method described in Fig. 1 to reconstruct them. However, it is worthwhile to notice the differences in the coordinate system. The positive *x*-axis directs to the north in the past RAMI phases, while the positive *y*-axis directs to the north in RAMI-V. Subsequently, the VAA and SAA are both counted from the north in each RAMI phase, but vary counterclockwise in the past RAMI phases while clockwise in RAMI-V. In addition, the number of the bands and sun geometries are also different from RAMI-3 to RAMI-V.
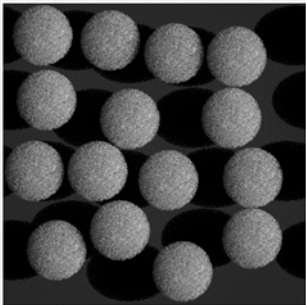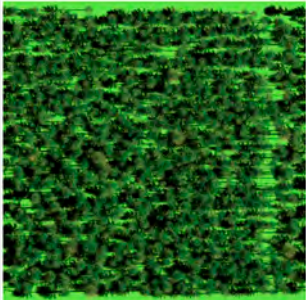
LESS RT model
As one of the 3D RT models, LESS was developed based on the ray tracing algorithm. LESS has been validated carefully by both the RAMI Online Model Checker (ROMC [51]) reference data and field measurements [1]. To date, LESS can simulate various RS observations and radiative budget, such as spectral images [28,36,52], BRFs [21,53], fluxes [7], the fraction of photosynthetically active radiation (FAPR [54]) absorbed by vegetation, and multi-platform LiDAR point clouds.

LESS provides 2 modes to simulate various RT observations and radiative budget demanded in RAMI-V (Table 2), including the FPT mode and BPT mode. The FPT mode can trace photons from the light sources to the sensors, which is convenient to simulate the albedo, FPAR, and BRF in the entire scene, particularly where the view geometry changes frequently. The BPT mode traces photons from the sensors (pixels) to the light sources in reverse, which is better for simulating all kinds of RS images. As seen from Table 2, RAMI-V demands a number of measurements. The flexible and easy-to-use Python interface wrapped by LESS can help batch simulations.

FPT in simulating albedo, FPAR, and BRF
In the FPT mode, LESS employs the actual and virtual photons to solve different RT problems. The actual photon is produced from a light source in a specific incident direction with power

Fig. 2. The spectral characteristics of each component in the scene HET07_JPS_SUM. The asterisk in the legend indicates the transmittance.

Table 1. Description of the example scenes selected from the past RAMI phases. The SAAs were converted to the coordinate system adopted by RAMI-V. The nadir orthographical images were respectively recolored with the normalized radiance in the NIR band for HET01 and RGB channels (R = 661 nm, G = 551 nm, B = 442 nm) for HET07.

Scene ID	Band	SZA	SAA	Nadir orthographic image
HET01_DIS_UNI	Red: 650 nm, NIR: 850 nm	20°, 50°	0°	
HET07_JPS_SUM	B01 to B18: 442 nm to 1,019 nm	36.6°	150.94°	

$P^0(\lambda)$ in wavelength λ. During propagation, the photon will intersect with the landscape elements and be scattered (reflected and transmitted). After intersection of Q times, the power of the photon will become

$$P^Q(\lambda) = P^0(\lambda) \cdot \prod_{q=1}^{Q} \left[\pi f(q, w_i, w_o, \lambda) / p_q \right], \qquad (1)$$

where $f(q, w_i, w_o, \lambda)$ is the bidirectional scattering distribution function (BSDF) at the qth intersection point, where the photon is scattered from incident direction w_i to outgoing direction w_o, and p_q is an empirical parameter that determines the probability of reflection or transmission. When p_q equals 0.5, half of the photons are reflected and the other half are transmitted, which is a trick that gives rise to qualitative (power) change rather than quantitative (number) change. In other words, a photon should have been reflected and transmitted at the same time, and 2 new photons with less power are generated. However, to avoid an exponential increase in the photon number, LESS assumes that a photon will choose to be either reflected or transmitted every time, and employs Monte Carlo sampling to achieve the approximate effect.

LESS places a virtual hemisphere Ω above the scene to receive escaped photons, and the albedo can be easily computed using

$$\alpha(\lambda) = \frac{\sum_{P^Q \in \Omega} P^Q(\lambda)}{P_{scene}(\lambda)}, \qquad (2)$$

where $P^Q \in \Omega$ means the actual photons escape out of the virtual hemisphere, and $P_{scene}(\lambda)$ is the power summary of all the actual

photons that enter the scene from the top. When all the incident light is direct, the albedo corresponds to the measurement *dhr*. Conversely, when all the incident light is diffuse, the albedo corresponds to the measurement *bhr*.

FPAR is the ratio of the absorbed PAR (APAR) to the incident PAR, where APAR accumulates from the absorbed power $P^Q(\lambda) - P^{Q-1}(\lambda)$ for each intersection by being integrated from 380 to 710 nm (PAR spectral region). FPAR can be shared by each canopy component as long as the classification label of each intersection point is recorded. Compared with the computation of FPAR, the measurements *fabs_fol* and *fabs_tot* resulted from 5 individual PAR bands (O03, O04, O05, O08, and O10) rather than the continuous spectral region due to band limitation.

The virtual photon is excited by an actual photon and received by a specific virtual detector along a virtual direction. In other words, once the actual photon is not completely absorbed, a virtual photon will be produced and sent to the virtual detector at every intersection point. Note that the virtual photons occluded by the landscape elements are invalid because they make no contribution to the detector and their power will become zero. Given that the zenith angle of the jth detector is θ_j and the total power collected by the detector in a unit solid angle is $I_j(\lambda)$, the directional BRF is derived from

$$\mathrm{BRF}(\lambda, \theta_j) = \frac{\pi I_j(\lambda)}{\cos\theta_j \cdot P_{scene}(\lambda)}. \qquad (3)$$

Similar to FPAR, total BRF can be further divided by the classification label and scattering order. Take the measurements

Table 2. Description of the RAMI-V measurements simulated by LESS.

Measurement	Sub-measurement	Definition	Solver
bhr	bhr	White sky albedo	FPT
dhr	dhr	Black sky albedo	FPT
fabs	fabs_fol	FPAR absorbed by the foliage	FPT
	fabs_tot	FPAR absorbed by the foliage and woody elements	
brfazim	brfazim	BRF in an azimuthal ring	FPT
brfpp	brfpp_total	Total BRF in the principle plane	FPT
	brfpp_co_sgl	BRF in the principle plane for being singly scattered by the vegetation	
	brfpp_mlt	BRF in the principle plane for being scattered twice or more	
	brfpp_uc_sgl	BRF in the principle plane for being singly scattered by the background	
brfop	brfop_total	Total BRF in the orthogonal plane	FPT
	brfop_co_sgl	BRF in the orthogonal plane for being singly scattered by the vegetation	
	brfop_mlt	BRF in the orthogonal plane for being scattered twice or more	
	brfop_uc_sgl	BRF in the orthogonal plane for being singly scattered by the background	
brf_sat	brf_olci	BRF for Sentinel-3 OLCI	FPT
	brf_modis	BRF for Terra MODIS	FPT
	brf_msi	BRF for Sentinel-2 MSI	BPT
thp	thp	Threshold hemispherical photograph (THP)	Ray intersection

brfpp and *brfop*, for example; their total quantities are distributed to the sub-components, including single scattering that occurred at the vegetation (*co_sgl*) or the background (*uc_sgl*) and multiple scattering (*mlt*). Regarding multiple scattering, the photons interacting twice or more with the landscape elements were considered in the computation of BRFs. As a consequence, the summary of BRFs from each sub-component should be equal to the total BRF, that is,

$$
\begin{aligned}
brfpp\_total &= brfpp\_co\_sgl + brfpp\_uc\_sgl + brfpp\_mlt \\
brfop\_total &= brfop\_co\_sgl + brfop\_uc\_sgl + brfop\_mlt
\end{aligned} \cdot \quad (4)
$$

### BPT in simulating BRF for MSI

Although FPT is good at simulating the BRFs over the entire scene under multiple view geometries, it is not suitable for the BRF simulation task for Sentinel-2 MSI (called *brf_msi*) because the observed target of *brf_msi* was not the entire scene but a part of the scene. It is confusing as to whether the reference plane (called the virtual plane in LESS) was still located above the scene like other BRF measurements. We believe that it is more reasonable that the field of view (FOV) of a satellite instrument is based on the ground rather than the top of the canopy. At least, the geographic position of the center of the observed target should remain unchanged. As seen from Fig. 3, when the virtual plane is located at the top of the canopy, 2

different regions, 1 (in blue) and 2 (in purple), are observed with the view geometry changing, which cannot promise positional consistency. Therefore, in order to finish this special task, we switched to the BPT mode to simulate spectral images, and then calculated an average BRF of the clipped images as *brf_msi* depending on the view geometries. It is notable that OLCI and MODIS were barely influenced by the virtual plane due to the copies of the entire scene, where the light exceeding the scene from one side will enter the scene from the opposite side again.

In the BPT mode, the ray is sampled from each pixel and scattered by the landscape elements along an inverse trajectory. For the *q*th intersection point, suppose that the incoming and outgoing radiance in wavelength λ are $L_i(q, \lambda, w_i)$ and $L_o(q, \lambda, w_o)$, respectively, where w_i and w_o are the corresponding incoming and outgoing directions. The rendering equation [55] below is used to establish a connection between $L_i(q, \lambda, w_i)$ and $L_o(q, \lambda, w_o)$ if the emission is not considered:

$$
L_o(q, \lambda, w_i) = \int_{4\pi} f(q, w_i, w_o, \lambda) L_i(q, \lambda, w_i) |\cos\theta_i| dw_i, \quad (5)
$$

where $f(q, w_i, w_o, \lambda)$ represents BSDF and θ_i is the angle between w_i and the normal at intersection point q. By doing recursion of Eq. 5 until the maximum scattering order is reached, we can obtain the radiance value of each pixel.
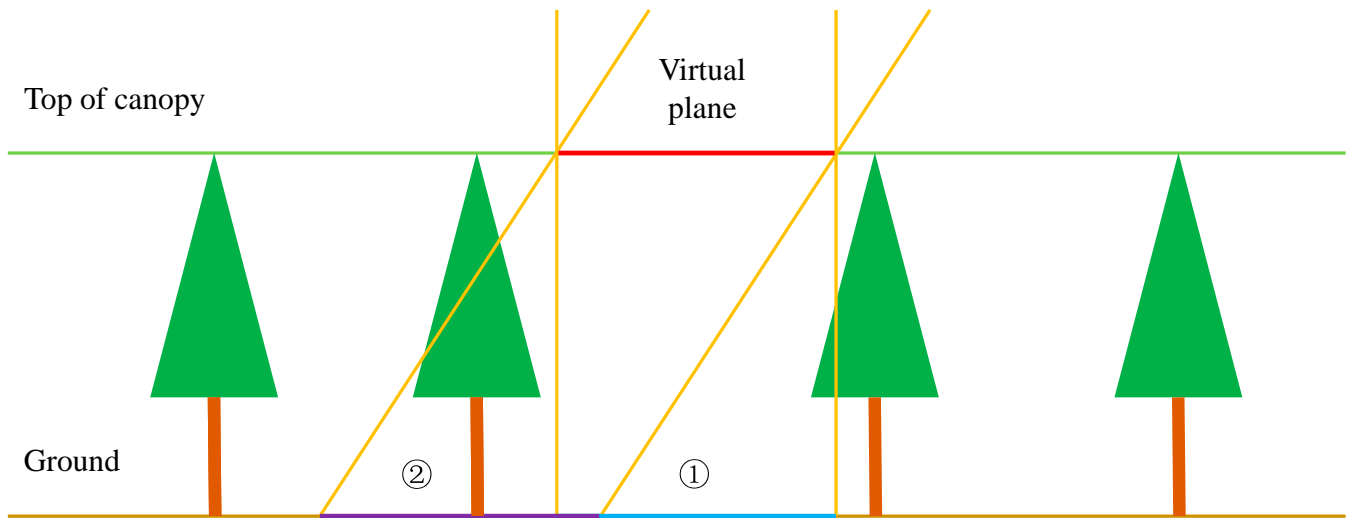
Fig. 3. The different FOVs determined by the virtual plane at the top of canopy with the view geometry changing. Region 1 in blue is observed at nadir direction and region 2 in purple is observed from the right side.

When simulating *brf_msi* in a fixed region, the corresponding pixels contained in the simulated images under different observation conditions inevitably differed. As a consequence, the clip operation was applied to the original simulated image whose area was larger than 20 m × 20 m (Fig. 4). Given that a clipping mask was created with 4 corners, the initial coordinates (Fig. 4A) of any corner were (x_{mask}, y_{mask}). When the sensor orbited around the scene (Fig. 4B to D), the coordinates were updated with

$$\begin{bmatrix} x'_{mask} \\ y'_{mask} \end{bmatrix} = \begin{bmatrix} 1 & 0 \\ 0 & \cos\theta_s \end{bmatrix} \cdot \begin{bmatrix} \cos\varphi_s & -\sin\varphi_s \\ \sin\varphi_s & \cos\varphi_s \end{bmatrix} \cdot \begin{bmatrix} x_{mask} \\ y_{mask} \end{bmatrix}, (6)$$

where θ_s and φ_s are the zenith angle and azimuth angle of the sensor (their initial values are 0), $\begin{bmatrix} \cos\varphi_s & -\sin\varphi_s \\ \sin\varphi_s & \cos\varphi_s \end{bmatrix}$ is a rotation matrix, which means the image is rotated by angle φ_s counterclockwise, and $\begin{bmatrix} 1 & 0 \\ 0 & \cos\theta_s \end{bmatrix}$ means the y-axial size of one pixel is divided by $\cos\theta_s$ because the larger θ_s is, the more objects can be observed.

THP and gap fraction

The original result of the measurement THP recorded the binary values (0/1), which identified sky visibility when looking up into 250,000 hemispherical directions from 9 given origins. Because THP was independent of the illumination conditions and spectra of architectural components, the computation of ray intersection was just enough. Although LESS did not embed the THP simulation function, thanks to the Python interface wrapped by LESS, it was still not hard to judge whether a ray sent from any position intersected with the landscape elements. Here, we attached more importance to how to exhibit the simulated results of THP. In fact, LESS had the ability to simulate multispectral digital hemispherical photographs, so a similar principle was applied to the exhibition of THP. Take equisolid

angle (a.k.a. equal area) projection, for instance; Eq. 7 was used to project the hemispherical coordinates formed by the zenith angle θ_{ray} and azimuth φ_{ray} (note that the north is 0) into the Cartesian coordinate system:

$$\begin{aligned} r &= 2f\sin\left(\frac{\theta_{ray}}{2}\right) \\ u_o &= \frac{r\sin\varphi_{ray}}{dx} \\ v_o &= \frac{r\cos\varphi_{ray}}{dy} \end{aligned}, (7)$$

where u_o and v_o are the pixel coordinates relative to the origin (the center of the image), f is the focal length, and dx and dy are the physical size of the pixel.

In order to obtain the directional gap fraction from the THP simulations, we first partitioned the canopy into several layers by 5° according to the zenith angle. In each layer, the directional gap fraction can be computed by:

$$P_{layer} = \frac{N_{sky}}{N_{layer}}, (8)$$

where N_{layer} and N_{sky} are the numbers of rays that enter the layer and touch the sky, respectively. If we set one layer whose zenith angle ranges from 0° to 90°, P_{layer} turns into the total gap fraction.

Accuracy indicators

Three indicators were selected to assess the accuracy of the simulation results from different aspects. They are the coefficient of determination (R^2), root mean square error (RMSE), and mean relative error (MRE), which can be used to evaluate the fitting accuracy, absolute accuracy, and relative accuracy, respectively. The larger R^2 or the smaller RMSE and MRE indicate the better agreement with the objective laws. Their computation was implemented by the equation below:
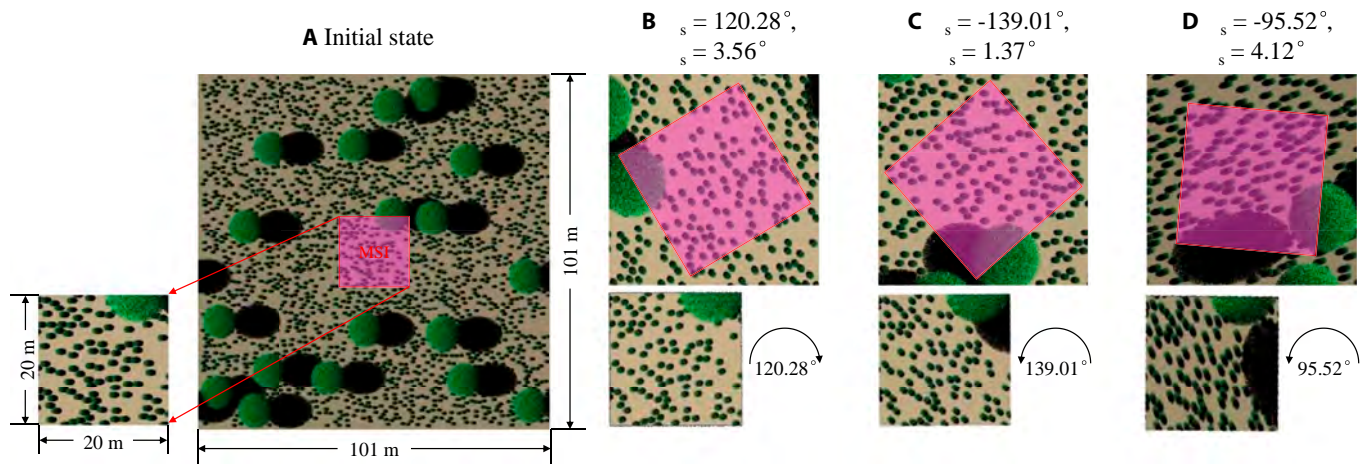
Fig. 4. Clip operation on the simulated radiance images of the scene HET16_DIS_S2S for *brf_msi*. Under different observation and illumination conditions (B to D), the rotated masks (the pink diamonds) refer to the basically identical region in the initial state (A).

$$R^2 = 1 - \frac{\sum_{i=1}^{n}(y_i - y_i^P)^2}{\sum_{i=1}^{n}(y_i - \bar{y})^2}$$

$$\text{RMSE} = \sqrt{\frac{1}{n}\sum_{i=1}^{n}(y_i - y_i^R)^2} \quad , \qquad (9)$$

$$\text{MRE} = \frac{1}{n}\sum_{i=1}^{n}\left|\frac{y_i - y_i^R}{y_i^R}\right| \times 100\%$$

where y is the simulated value, y^P is the predicted value, y^R is the reference value (e.g., the ROMC reference data, high-accuracy simulated data), $\bar{y}$ is the mean, and n is the number of samples excluding those whose y values are zero in the MRE computation.

Results

BRF simulations

As RAMI-V involved numerous scenes and measurements, obviously, it is tedious to illustrate all the simulation results. Hence, in this section, the BRF and its related measurements were illustrated, including the BRF in the principal plane (*brfpp*), orthogonal plane (*brfop*), and azimuthal ring (*brf_azim*) as well as the BRF for the satellite instruments (*brf_sat*). In addition, 8 representative scenes were selected from different groups shown in Table S1, among which HOM29 and HET16 represent abstract scenes, HET07 is chosen as an example of coniferous forests, HET09 and HET15 are combined to represent broad-leaved forests in different seasons, HET14 is characterized by row structure, and the new actual scenes in RAMI-V are necessary to be included.

BRF in the principle plane and orthogonal plane

Figure 5 depicts examples of the *brfpp* and *brfop* simulations with specific sun geometries. The first and second rows of each scene show the proportions of 3 sub-components to total *brfpp* and *brfop*, respectively. The hot spot regions of most scenes are narrow and sharp, importantly, corresponding to the SZAs, except for HET09 and HET15, whose SZAs were set as even degrees whereas VZAs were all sampled at odd degrees. Let us pay more attention to *brfpp_co_sgl*, whose tendency basically

agrees with *brfpp_total* in a large part of the scenes. Exceptionally, the *brfpp_co_sgl* area of HET15 and HET50 tends to shrink, and even the BRF values in the hot spot regions are not maximum. According to the simulated 4-component products shown in Fig. 6, it is not hard to find a reason that a larger area of illuminated vegetation can be observed at larger VZAs to explain these unusual cases. Compared with leaf-on HET09 (Fig. 6A to C), the vertically elongated woody elements in HET15 (Fig. 6D to F) can be seen more in a large-angle view due to the loss of foliage. For HET50, its dominant vegetation is made up of grasses whose leaf angles obey the erectophile distribution [56] (Fig. 7) featuring similar interception regulation to the woody elements.

The *brfop* curves in the middle panel show good symmetry except for HET14. This is because the observation direction is neither parallel nor perpendicular to the orientation of the plant rows in HET14 (imagine there is a VZA offset that makes the curve symmetrical). Although some of the *brfop_total* curves are bowl-shaped and some are bell-shaped, the *brfop_uc_sgl* curves are always bell-shaped (high in the middle and low on both sides). In most cases, the reflectance anisotropy of vegetation (*brfop_co_sgl*) is characterized by a bowl shape except that the shape of the *brfop_co_sgl* curve in HET51 is like a bell.

The bottom panel displays the BRF values of the total and sub-components at the hot spots in different bands. The first impression of these charts is that 2 peaks corresponding to green and NIR bands, as well as one obvious valley corresponding to the red band, occur in the *brfpp_total* and *brfpp_co_sgl* simulations, which is dominated by the foliage spectra. HET15 and HET50 are still exceptions, whose trends of *brfpp_co_sgl* depend on the non-foliage dominant vegetation: woody elements and grasses, respectively.
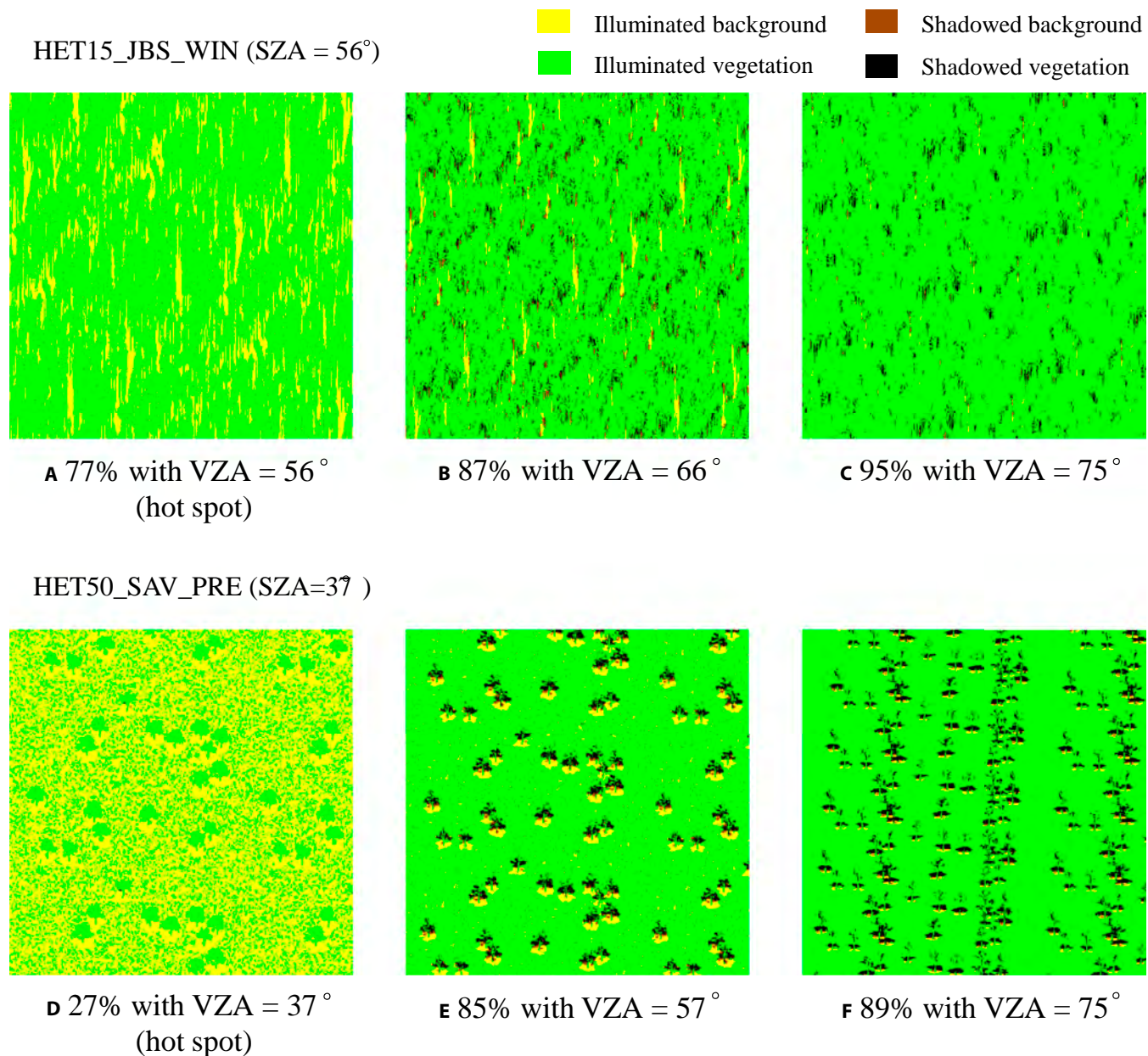
BRF in an azimuthal ring

The *brf_azim* simulations demanded a fixed VZA (equal to 37°) and VAAs sampled at 2° intervals ranging from 0° to 358° or 1° to 359°. Figure 8 depicts several curves representing *brf_azim* simulations in the NIR (O17), red (O08), green (O06), and blue (O03) bands. Overall, the shapes of these 4-band curves remain consistent with each other in every example scene. Moreover, the rank relationships of these curves between the 4 bands' response to those charts are shown in the
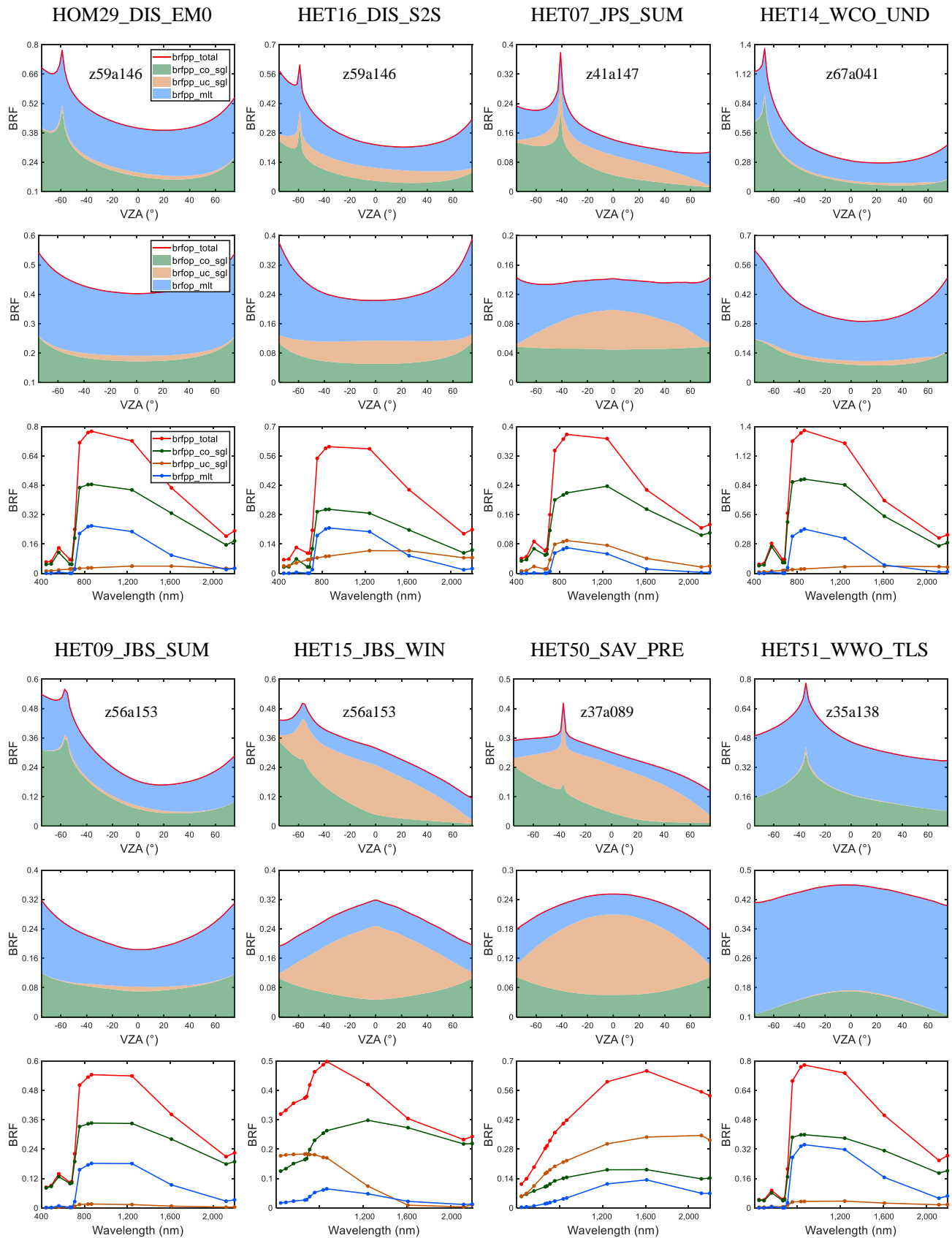
Fig. 5. The *brfpp* and *brfop* simulations in 8 representative scenes. For each scene, top to bottom displays the *brfpp* proportions of 3 sub-components, the *brfop* proportions of 3 sub-components, and the BRFs at hot spots in 13 bands. The area in different colors represents the proportions coming from the BRFs in the NIR band (O17). The label zXXaXXX means SZA = XX° and SAA = XXX°.

HET15_JBS_WIN (SZA = 56°)

Illuminated background   Shadowed background
Illuminated vegetation   Shadowed vegetation

A 77% with VZA = 56°
(hot spot)

B 87% with VZA = 66°

C 95% with VZA = 75°

HET50_SAV_PRE (SZA=37°)

D 27% with VZA = 37°
(hot spot)

E 85% with VZA = 57°

F 89% with VZA = 75°

Fig. 6. The area ratio of the illuminated vegetation derived from 4-component products in HET15 (A to C) and HET50 (D to F) with the VZA increasing in back scattering directions.

bottom rows in Fig. 5. For example, in HET50, the *brfpp_total* values at hotspots are ranked in ascending order from the blue band to the NIR band, while the brf_azim values maintain this rank relationship (NIR > red > green > blue). The straight lines connecting hot spots (although the zenith angles differ) in each band indicate the bulges of these curves. It is not surprising that the markers of the sun are just right on the lines in most scenes, even though there is a slight bias in HET14. Inspired by RAMI-IV, Fig. 9 reveals some interesting phenomena in the row structure. Different from the experiments above, the SAA and SZA were forced to be 0° and 37°, respectively (Fig. 9A). Therefore, Fig. 9B depicts a true hot spot where the BRF value is maximum, the pixels in the 4-component product are all illuminated, and the normalized radiance image is the brightest. Since the plant rows in HET14 are north–south directional, apart from occlusion in the vegetation, a small area of the

background near the ends of the rows is occluded looking from the opposite side in Fig. 9D. In contrast, when the observer stands on the west or east side in Fig. 9C, a larger area of the background on the side of the rows is occluded depending on the height of the rows; thus, the BRF value is smaller than that in Fig. 9D.

BRF for satellite instruments
This is a new simulation type in RAMI-V. Distinguished from the general BRF simulations mentioned above, the *brf_sat* simulations were sampled with 4 parameters, where both the sun geometry and the view geometry vary. In order to better illustrate the simulations, the independent variable is replaced by the date referencing the RAMI website.

Figure 10A to C are designed to probe the differences in the *brf_sat* and normalized difference vegetation index (NDVI) varying with the latitude (only for abstract scenes). The NDVI was

derived from [NDVI = (BRF$_{O17}$ − BRF$_{O08}$)/(BRF$_{O17}$ + BRF$_{O08}$)]. Due to Earth's revolution around the Sun, the change in the SZA in the north (increase first and then decrease) is opposite to those in the south (decrease first and then increase) throughout the year. Therefore, it is obvious that the changes in *brf_sat* in the
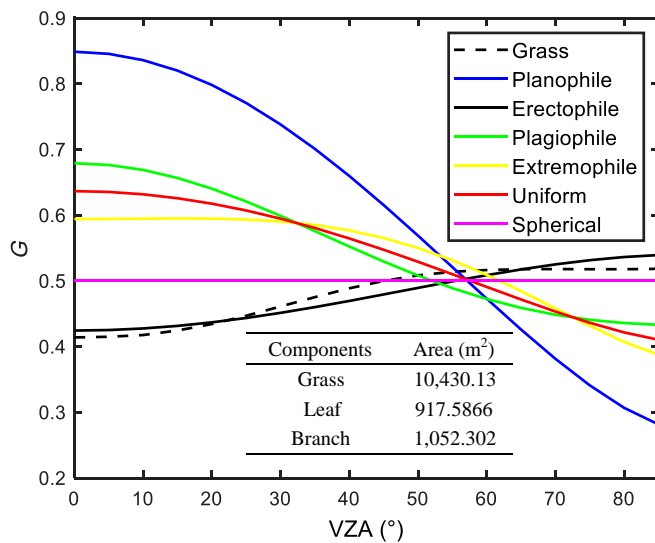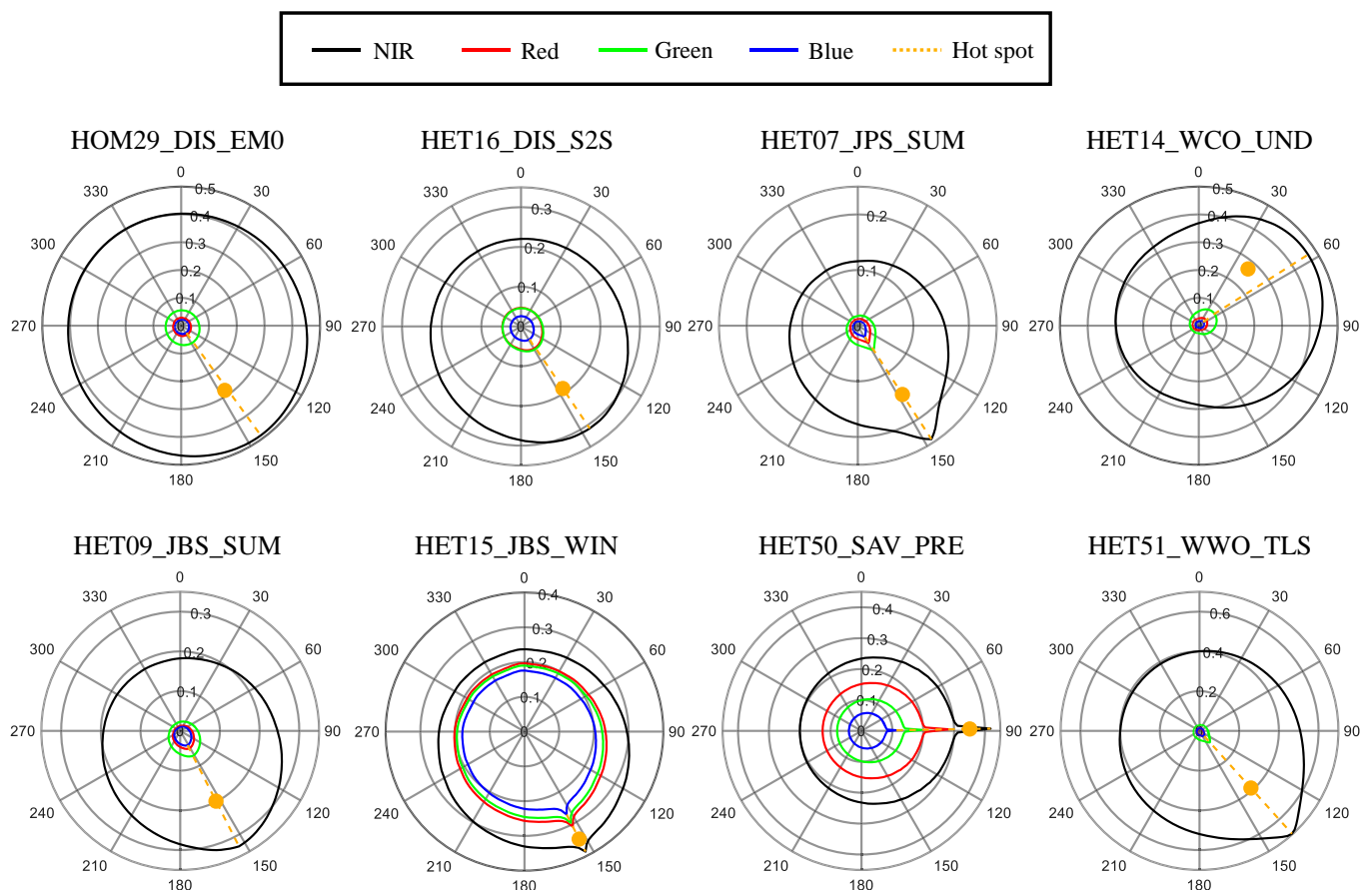
red band and NDVI are contrary between latitudes 30°N and 30°S. In January, the SZAs in latitude 30°S reach the lowest level, and the corresponding BRFs in the red band are larger and NDVIs are smaller. In July, the case in latitude 30°S is the reverse. In a word, the BRF in the red band and NDVI are both greatly affected by the SZA.

Figure 11 is aimed at exploring the influence of the view geometry and leaf area index (LAI) on the NDVI given that the sun geometry basically varies slightly within a month. First, the NDVIs at various LAI levels are all more or less wavy (Fig. 11A), which can be attributed to the change in the view geometry. Then, the standard deviation decreases with the LAI increasing (Fig. 11B). That is, the NDVI in the sparse vegetated areas is more sensitive to the view geometry than that in the dense vegetated areas. Thus, we should pay more attention to the view geometry when using NDVI to retrieve vegetation parameters, especially for sparse vegetation.

Figure 12A to C are used to compare the changes in *brf_sat* and NDVI between 2 scenes (HET 15 and HET09) in different seasons, keeping the view and sun geometries the same. Overall, the BRF values in winter (leaf-off HET15) are larger than those in summer (leaf-on HET09) in the red band. It is confusing that this relationship still exists in the NIR band except for OLCI and MODIS in January, which is attributed to a high-reflectivity snowy background in winter. Based on this, we wondered whether the NDVI, which indicates the growing state of vegetation, is affected by a snowy background. It turns out


Fig. 7. The total area of each structural component and the *Gs* (projection coefficients) derived from typical leaf angle distributions and the dominant grasses in HET50.

Fig. 8. The *brf_azim* simulations in 8 representative scenes. The orange lines were drawn by connecting the maximums of *brf_azim* in each band. The orange markers represent the sun under the corresponding illumination conditions that are the same as those used in Fig. 5.
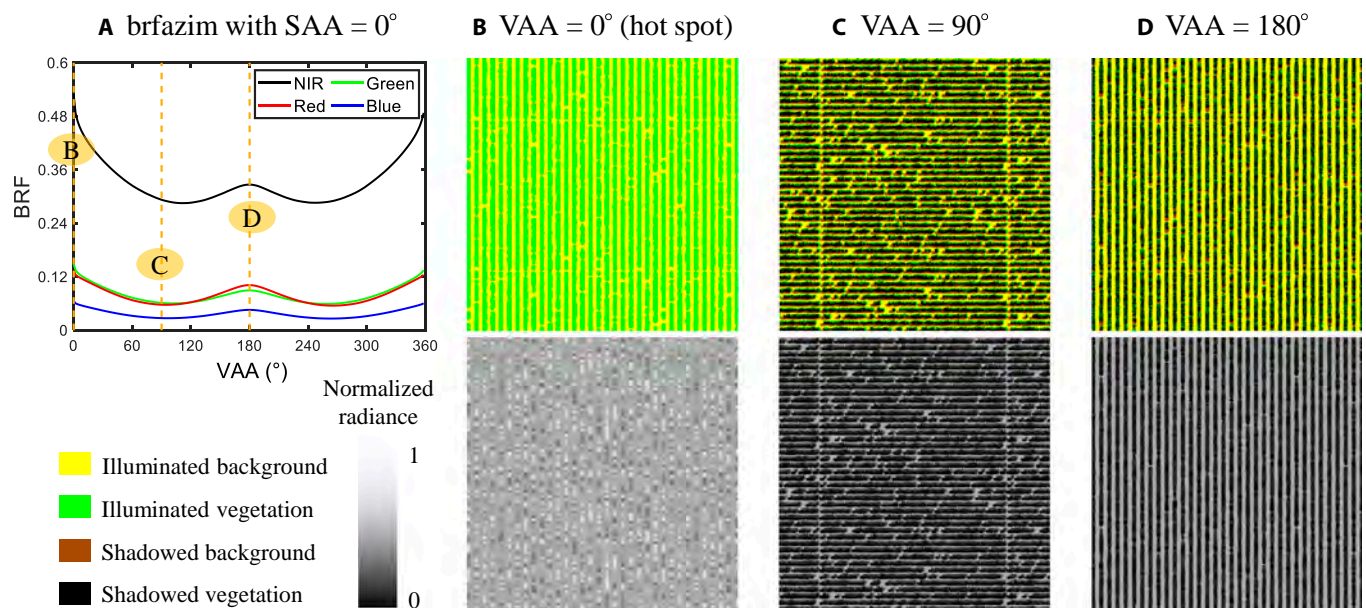
Fig. 9. The explanation for the change in the *brfazim* simulation in HET16. Regarding plots (B) to (D), the first and second rows display simulated 4-component products and normalized radiance images (ranging from 0 to 1), respectively. The bands in plot (A) are the same as those in Figure 8. Note that the VZA and SZA are both 37°.
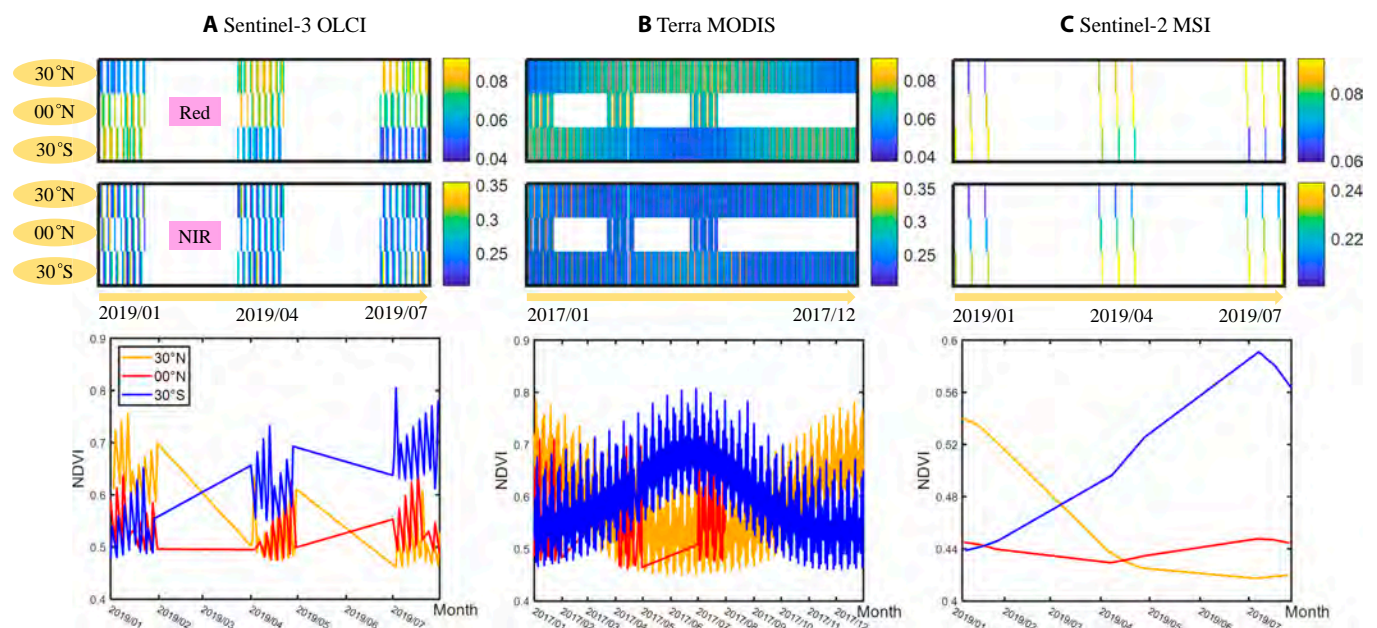
Fig. 10. The simulated *brf_sat* in the red (upper part of the top panel) and NIR (lower part of the top panel) bands as well as the NDVI (bottom) results for 3 satellite instruments (A to C) in different latitudes in HET16.

that the NDVIs in summer are always far beyond those in winter for whichever satellite instrument.

Energy conservation in absorption and albedo

According to energy conservation, the incident radiance energy is either absorbed by the landscape elements or scattered out of the scene. Albedo is a flux quantity explaining the scattered proportion of the radiance energy. However, unlike the purist scenario presented in RAMI-3 and RAMI-IV, which satisfied conservative scattering conditions (the reflectance of the background equaled 1), not only the vegetation but also the background contribute to the absorption in the RAMI-V scenes. Since

the measurement *fabs_tot* can only explain the former part, it is difficult to validate energy conservation using only *fabs_tot* and albedo simulations in the true sense. A useful solution is to select some special scenarios to eliminate the effects on absorption caused by the background. These scenarios are under the conditions that (a) the reflectance of the background in the PAR spectral region is close to 1, or (b) the vegetation is so dense that the light can barely reach the background. The first condition is only used for those scenarios whose background is covered by snow, e.g., HET08_OPS_WIN and HET15_JBS_WIN. For the second condition, the nadir orthographic images shown in Table S1 help to visually judge whether the vegetation is dense enough. A large
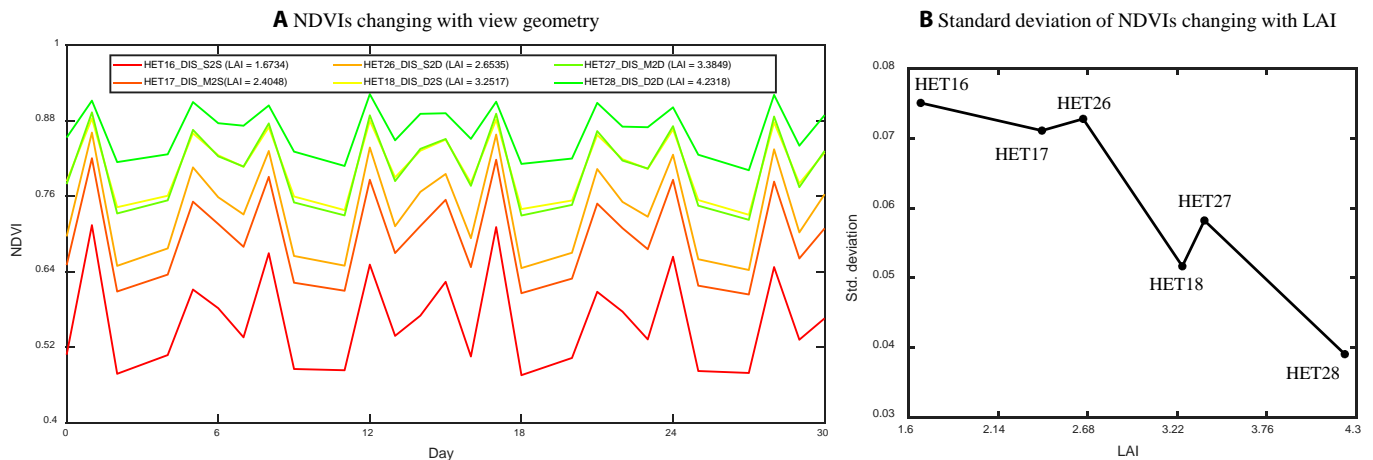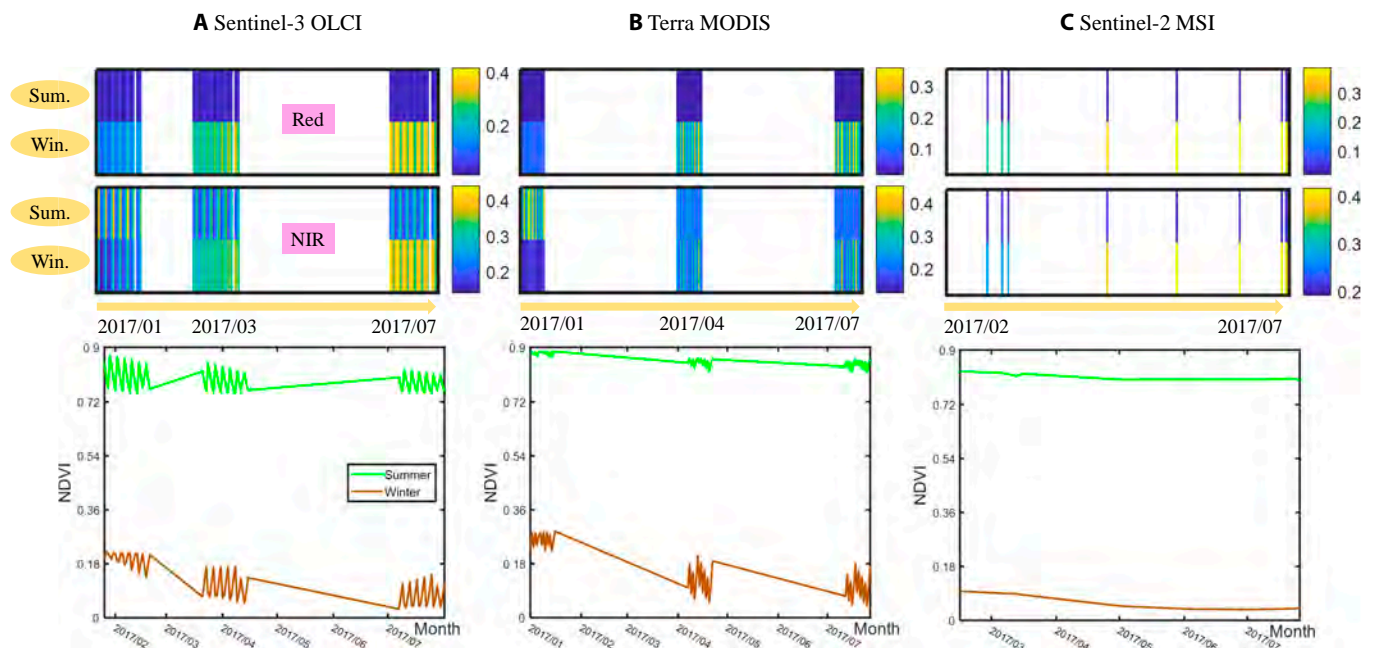
A NDVIs changing with view geometry

B Standard deviation of NDVIs changing with LAI

Fig. 11. The changes in the NDVI (A and B) for MODIS in latitude 00°N in July in the abstract scenes at different LAI levels.

A Sentinel-3 OLCI **B** Terra MODIS **C** Sentinel-2 MSI

Fig. 12. The simulated *brf_sat* in the red (upper part of the top panel) and NIR (lower part of the top panel) bands as well as NDVI (bottom) results for 3 satellite instruments (A to C) in the scenes HET09 and HET15, which represent forests in summer and winter, respectively.

part of the scenes is filtered except HOM26_DIS_EPD and HOM36_DIS_PED. Overall, Fig. 13A illustrates good consistency ($R^2 = 99\%$, interception = 0.99) between *fab_tot* plus albedo and 1 in each PAR band under the 2 kinds of illumination conditions (direct or diffuse light). The slopes of Fig. 13D and E have greater biases against −1, and the R^2 values of Fig. 13B and C are relatively smaller because of the imperfections of the selected scenes.

Gap fraction

The directional gap fraction and total gap fraction were derived from the THP simulations according to Eq. 8. In terms of the structure, the difference between the scenes HET09 and HET15 only lies in whether the broad-leaved trees have foliage or not. Therefore, there is a big difference in LAI between HET09 and HET15 resulting from the season. Beer's law [57] describes a functional relationship between the gap fraction and LAI. Figure 14 shows that the directional gap fraction in winter is larger than that in summer in almost every layer, which intuitively explains Beer's

law. RAMI-V defined the sample number of the THP simulation as 250,000. In fact, when the sample number reaches 150,000, the total gap fraction is stable enough (the standard deviation is very small in Fig. 15). In other words, the probability that the total gap fraction sampled singly with the amount of 150,000 is close to that sampled singly with the amount of 250,000 is quite large.

Simplification schemes of structure

The Canopy structure section lists some simplified basic geometries applied to the LESS simulations. There is a question about how different simplification schemes will affect the simulation accuracy. Here, we will introduce 2 kinds of simplification schemes: the surface-area-unchanged (SAU) scheme and the radius-unchanged (RAU) scheme (Fig. 16). For instance, when a disc needs to be simplified as an *X*-sided regular polygon, the RAU scheme will adopt an inscribed polygon to ensure that the radius of this disc remains unchanged, while the SAU scheme will properly enlarge the radius until the surface area

A Overall fit

B HOM26_DIS_EPD

C HOM36_DIS_PED

D HET08_OPS_WIN

E HET15_JBS_WIN
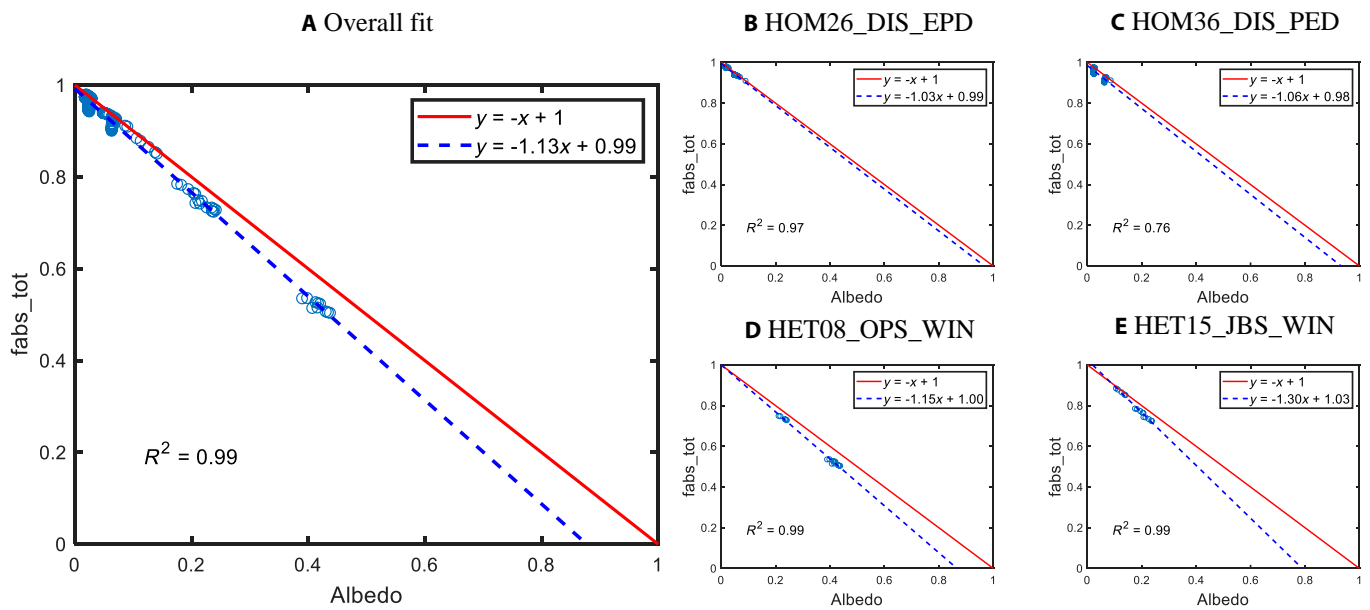
Fig. 13. The relationship between *fabs_tot* and albedo (A to E). The albedos include white (*bhr*) and black (*dhr*) sky albedos in 5 individual PAR bands. The red solid lines in each plot are the reference lines, where *fabs_tot* plus albedo is equal to 1. The blue dashed lines in each plot were fitted by the samples selected from the corresponding scene.
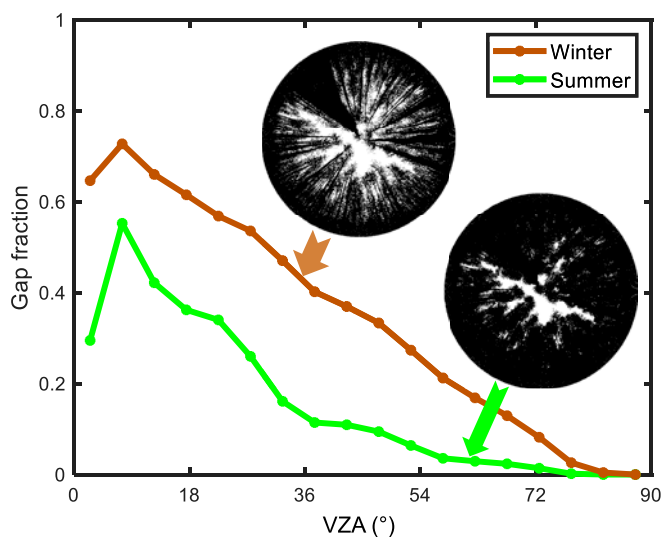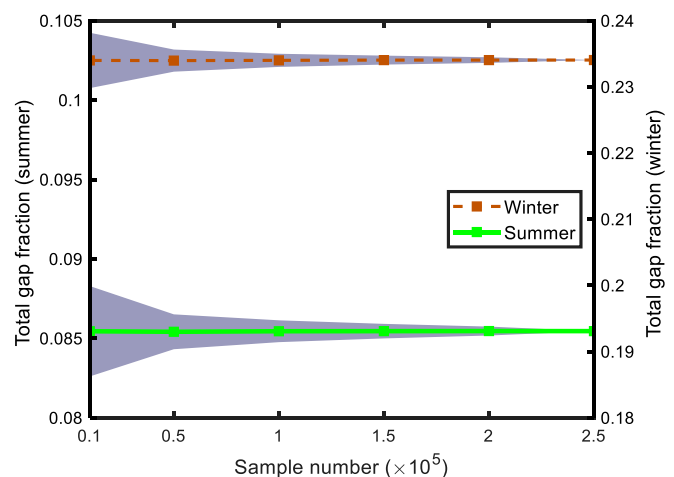

Fig. 14. The directional gap fraction and THPs in 2-season JBS scenes. The THPs projected using Eq. 7 are binary images, where the black and white pixels only mean an invisible and visible sky.

Fig. 15. The means (the solid lines) and standard deviations (the purple area) of the total gap fraction sampled 1,000 times at different sample numbers from the THP simulations in 2-season JBS scenes.

of the polygon remains the same as that of the disc. Obviously, these 2 schemes are equivalent only if X is infinite.

Validation with ROMC and Rayspread

To validate 2 kinds of simplification schemes above, we used the ROMC reference data for RAMI-3 abstract scenes and compared it with the RT model Rayspread for RAMI-IV actual scenes. The example scenes HET01_DIS_UNI and HET07_JPS_SUM represent the abstract and actual scenes, respectively.

For HET01_DIS_UNI, the disc is the only 2-dimensional geometry. The simplification relies on the number of edges of the X-sided regular polygon. X was set to 4, 6, 8, 12, 16, and 20. The simulation results of *brfpp_total* with different Xs were

compared with the ROMC reference data under the SAU and RAU schemes. As seen from Fig. 17, the SAU errors always remain at a lower level whatever X is, while the RAU errors almost decrease with X. In general, the SAU scheme can achieve good accuracies with smaller Xs, which saves storage size because the storage size of the OBJ file was proportional to X. In addition, when X is equal to or greater than 16, the errors in the red band become small and stable, even though errors in the NIR band is a little wavy within a narrow range. Therefore, we might as well take $X = 16$ as the reference when the official reference data are not available, such as RAMI-V. When X is greater than 8, the RAU scheme is even superior to the SAU scheme in the NIR band. However, their errors gradually get close to each
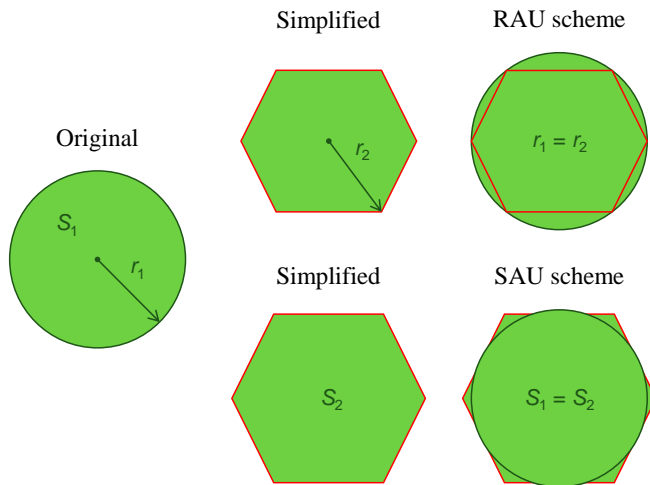
Fig. 16. Two different simplification schemes. The symbols *r* and *S* represent the radius and area of the corresponding geometries, respectively.
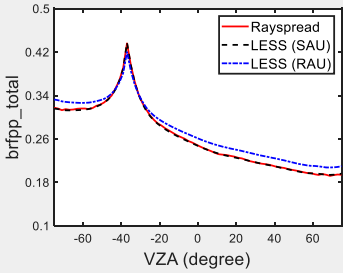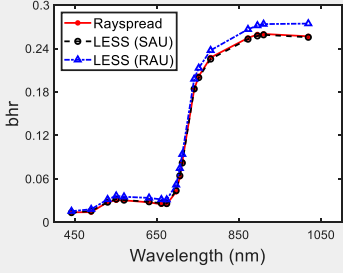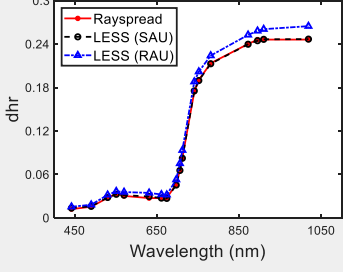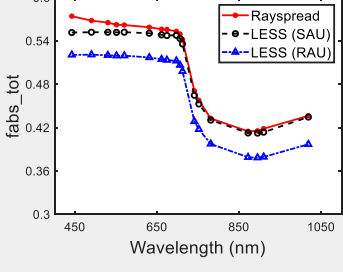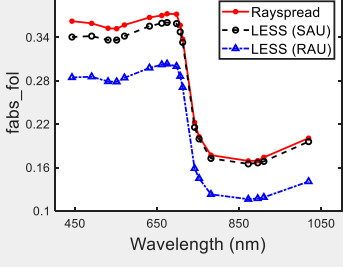
other after $X = 12$, which indicates that the ROMC reference data may deviate from the truth because it simply takes averages of the simulation results of some credible 3D Monte Carlo RT models.

The surface area is equally essential for the 3D geometries used in the actual scenes because there is a close relationship between the average projected area over all the possible view angles and the surface area for the convex bodies [49]. Meanwhile, the projected area plays a very important role in the retrieval of structural parameters, such as LAI. Therefore, there still exists a dilemma of choosing simplification schemes with respect to the actual scenes. Unfortunately, the ROMC has not provided the reference data for RAMI-IV actual scenes. Thus, we chose one of the credible 3D RT models, Rayspread, as the reference to compare the performance of 2 simplification schemes on actual scenes. Rayspread employs constructive solid geometries (CSG) techniques, which can reconstruct RAMI scenes without simplifications. Note that Rayspread and LESS both did simulations in the FPT mode, and the secondary ray mechanism in Rayspread was also used in LESS (called virtual photons). Table 3 illustrates that the SAU errors are far less than the RAU errors for any measurement.
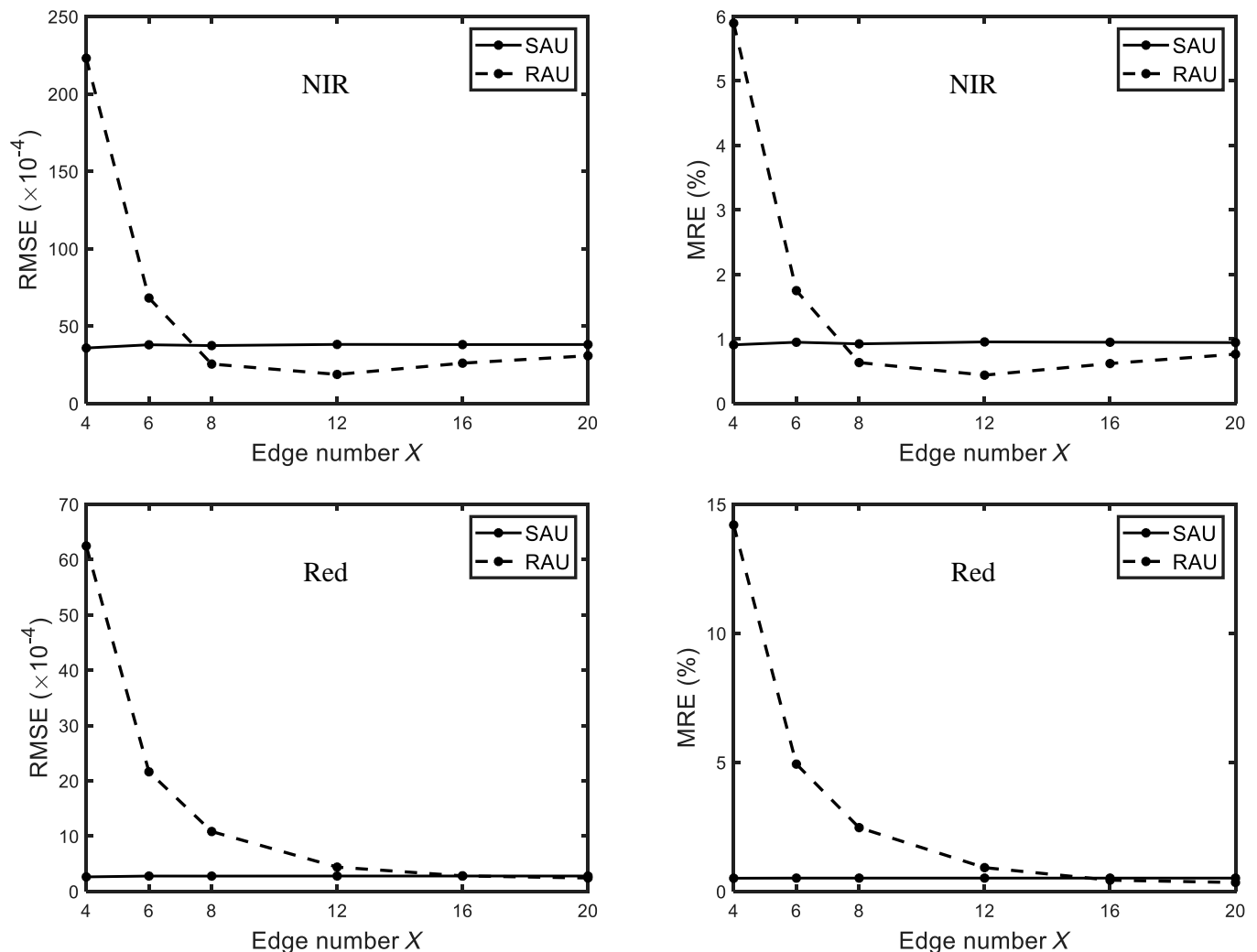
Fig. 17. The RMSEs and MREs of *brfpp_total* in the red and NIR bands among different *X*s under all the illumination conditions with respect to HET01_DIS_UNI using the SAU and RAU schemes.

Table 3. The RMSEs ($\times 10^{-3}$) and MREs (%) of the typical measurements under all the illumination conditions with respect to HET07_JPS_SUM using the SAU and RAU schemes. The *brfpp_total* example was drawn with SZA = 36.6° and band = B16 (895 nm).

Measurement	SAU		RAU		Example
	RMSE	MRE	RMSE	MRE	
brfpp_total	1.04	0.85	7.79	10.83	
bhr	1.40	2.59	9.94	14.31	
dhr	0.97	2.21	9.70	12.75	
fabs_tot	9.31	1.44	42.02	8.24	
fabs_fol	11.50	3.23	66.28	23.92	

The SAU scheme performs very well on the BRF and albedo simulations, which are very close to the Rayspread simulations. Although 2 schemes both have biases against Rayspread for the absorption simulations, the SAU scheme produces more similar results to Rayspread due to consistency of the surface area.

Table 4. The RMSEs ($\times 10^{-4}$) and MREs (%) of the typical measurements among different Xs ($X = 16$ is the reference) under all the illumination conditions using the SAU scheme. The asterisk indicates the smallest RMSE or MRE.

Scene	Measurement	$X = 4$		$X = 6$		$X = 8$		$X = 12$	
		RMSE	MRE	RMSE	MRE	RMSE	MRE	RMSE	MRE
HOM29	brfpp_total	5.07	0.14	2.18	0.05	1.59	0.03	1.32*	0.02*
	bhr	0.88	0.03	0.47*	0.03*	1.28	0.04	0.98	0.05
	dhr	1.72	0.08	1.46	0.04	1.11*	0.04	1.52	0.03*
	fabs_tot	1.63	0.02	0.95	0.01	0.86	0.01	0.65*	0.00*
HET16	brfpp_total	21.59	0.24	0.94	0.02	0.92	0.02	0.79*	0.02*
	bhr	0.98	0.03	0.47	0.03*	0.44	0.04	0.30*	0.03
	dhr	8.25	0.14	0.94	0.03	0.71	0.03	0.62*	0.02*
	fabs_tot	1.17	0.02	0.71	0.01	0.95	0.01	0.59*	0.01*

Table 5. The RMSEs ($\times 10^{-4}$) and MREs (%) of typical measurements among different Xs under the same conditions as Table 4 but using the RAU scheme. The asterisk indicates the smallest RMSE or MRE.

| Scene	Measurement	$X = 4$		$X = 6$		$X = 8$		$X = 12$	
		RMSE	MRE	RMSE	MRE	RMSE	MRE	RMSE	MRE
HOM29	brfpp_total	239.64	8.99	89.66	3.28	42.38	1.54	10.56*	0.39*
	bhr	208.26	8.32	78.19	3.00	37.09	1.45	11.00*	0.37*
	dhr	209.35	8.51	77.44	3.07	36.98	1.44	9.64*	0.37*
	fabs_tot	848.95	11.61	312.26	4.26	148.69	2.03	37.72*	0.51*
HET16	brfpp_total	119.65	7.81	46.30	2.80	22.48	1.32	5.77*	0.33*
	bhr	72.31	7.60	25.78	2.62	12.50	1.25	3.53*	0.34*
	dhr	72.61	7.57	26.49	2.63	12.63	1.23	3.40*	0.31*
	fabs_tot	437.63	10.92	147.40	3.69	67.81	1.70	16.64*	0.42*

Performance on RAMI-V scenes

The SAU scheme has been validated with ROMC and Rayspread for RAMI-3 and RAMI-IV scenes. Nevertheless, only 2 representative scenes were tested and the sun geometries in the past RAMI phases were not adequate. Here, we compared the performance of 2 simplification schemes with more abstract and actual scenes from RAMI-V.

For the abstract scenes, HOM29_DIS_EM0 and HET16_DIS_S2S were taken as examples. X was set to 4, 6, 8, 12, and 16, and $X = 16$ was taken as the reference. The simulation results with different Xs under the SAU scheme are evaluated in Table 4. It is obvious that most errors (both RMSEs and MREs) decrease with X increasing, and reach the smallest when X is equal to 12. However, the errors are basically unchanged for HET01 in Fig. 17. This is because the more sun geometries defined in RAMI-V amplify the differences among

Xs. Although some of the smallest RMSEs and MREs are not from the last column in Table 3, it is still reasonable because the errors are so small when X is greater than 6 that some random sampling errors are inevitable in the simulations. That is to say, the level of the simulation errors with different Xs is equivalent to those random sampling errors, thus, the simulation accuracy is acceptable when X is greater than 6.

When we switched to the RAU scheme, X was still set to 4, 6, 8, 12, and 16, respectively. The simulations with different Xs were quantitatively compared with those with $X = 16$. It can be obviously seen from Table 5 that the errors are dramatically large when X is small, and decrease quickly with X increasing. However, the RMSEs and MREs with $X = 12$ are still at least 10 times greater than those under the SAU scheme, which is different from Fig. 17 where the RAU scheme performs better than the SAU scheme when X is large. Certainly, the accuracies
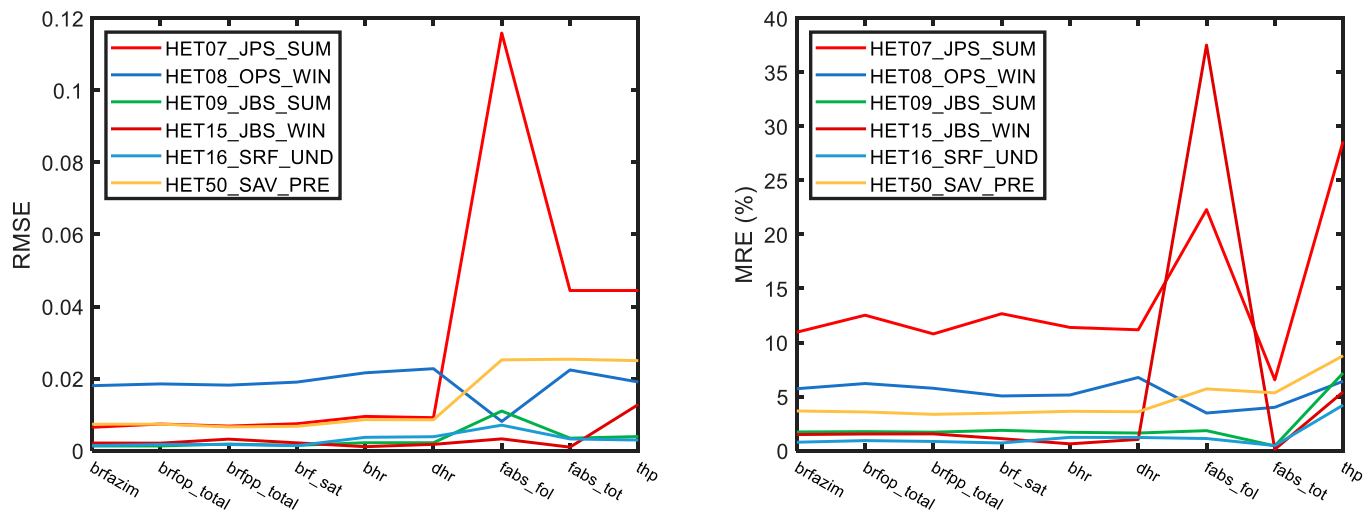
Fig. 18. The RMSEs and MREs between 2 schemes SAU and RAU under all the observation and illumination conditions with respect to each actual scene. The errors of THP simulations were computed with directional gap fraction defined in Eq. 8.

Table 6. The LAIs and PAIs under 2 different simplification schemes SAU and RAU in the representative actual scenes.

| Scene	LAI (SAU)	PAI (SAU)	LAI (RAU)	PAI (RAU)
HET07_ JPS_SUM	2.2839	3.3870	1.4375	2.4029
HET08_ OPS_WIN	0.6678	1.0553	0.4309	0.7710
HET09_ JBS_SUM	3.4552	5.1921	3.4527	5.0572
HET15_ JBS_WIN	0.0336	1.6894	0.0230	1.6275
HET16_ SRF_UND	3.2086	3.7832	3.2086	3.7410
HET50_ SAV_PRE	1.1348	1.2400	1.0378	1.1430

will be improved with X further increasing under the RAU scheme, but it needs to store bigger OBJ files and parse more triangles to construct the scenes, which will be bound to increase the computational burden in LESS simulations. Therefore, comparing with the RAU scheme, the SAU scheme is recommended for the abstract scenes because it can effectively avoid adding complex geometries but still maintain the simulation accuracy.

RAMI-V has provided 8 actual scenes. If the structural definition only contains triangles, there is no structural difference between different simplification schemes; thus, the actual scenes HET14 and HET51 were filtered. Figure 18 illustrates the differences between the aforementioned 2 schemes for the remaining actual scenes taking the SAU scheme as the reference. Overall, HET07 is the most differential scene, in particular, for the measurements *fabs_fol*, *fabs_tot*, and *thp*, while the errors of measurement *fabs_fol* are dramatically large for HET07 and HET15. The *fabs_fol* and *fabs_tot* are quantities

concerned with FPAR, and *thp* is quantified by directional gap fraction. They are all closely related to LAI [58,59], especially for HET15 (leaf-off), where LAI is replaced by plant area index (PAI). As illustrated in Table 6, the LAIs and PAIs derived from the SAU and RAU schemes differ the most in HET07; therefore, the measurements *fabs_fol*, *fabs_tot*, and *thp* are the worst. In addition, since LAI in HET15 is very small, the absolute difference is only approximately 0.01, whereas the relative difference is approximately 1/3, which gives rise to the large MRE of the measurement *fabs_fol*.

Illumination resolution

LESS defined the illumination resolution to determine the number of ray samples in the FPT mode. When it is set to k, a number of rays will be emitted at intervals of k meters. In other words, $1/k$ rays will be produced in a unit length. More ray samples mean more times of intersection computation, which finally results in low efficiency. Here, we selected 2 representative scenes, HET16_DIS_S2S (Fig. 19A) and HET51_WWO_TLS (Fig. 19B), to figure out how the illumination resolution affects the simulation accuracy and speed of the BRF, albedo, and absorption on earth. All the simulations were run on a workstation with Intel(R) Xeon(R) Silver 4110 CPU @ 2.10 GHz 64.0 GB. Figure 19 depicts the changes in the time and accuracy following 1, 10, 25, 50, 100, and 200 ray samples (k = 1, 0.1, 0.04, 0.02, 0.01, and 0.005, respectively). The time cost polylines in the first column all illustrate a dramatic increase after 50 ray samples. It is interesting that some time cost polylines in Fig. 19B do not start from the origins because it took more time to load the more complex HET51 than the abstract HET16; therefore, the actual simulation time was ignored. In most cases, the errors remain at a low level after 10 ray samples, stabilize after 25 ray samples, and approach zero after 50 ray samples. Even though the errors of the *fabs_tot* simulations in Fig. 19B are slightly wavy, the MREs and RMSEs are below 0.06% and 0.0006, respectively. The scatter charts in the last column indicate that the simulation results for 50 ray samples (k = 0.02) are basically equal to those for 200 ray samples (k=0.005) no matter what the measurement is. To conclude, 50 ray samples is an optimal choice to perform accurate simulations in an acceptable time.

A HET16_DIS_S2S
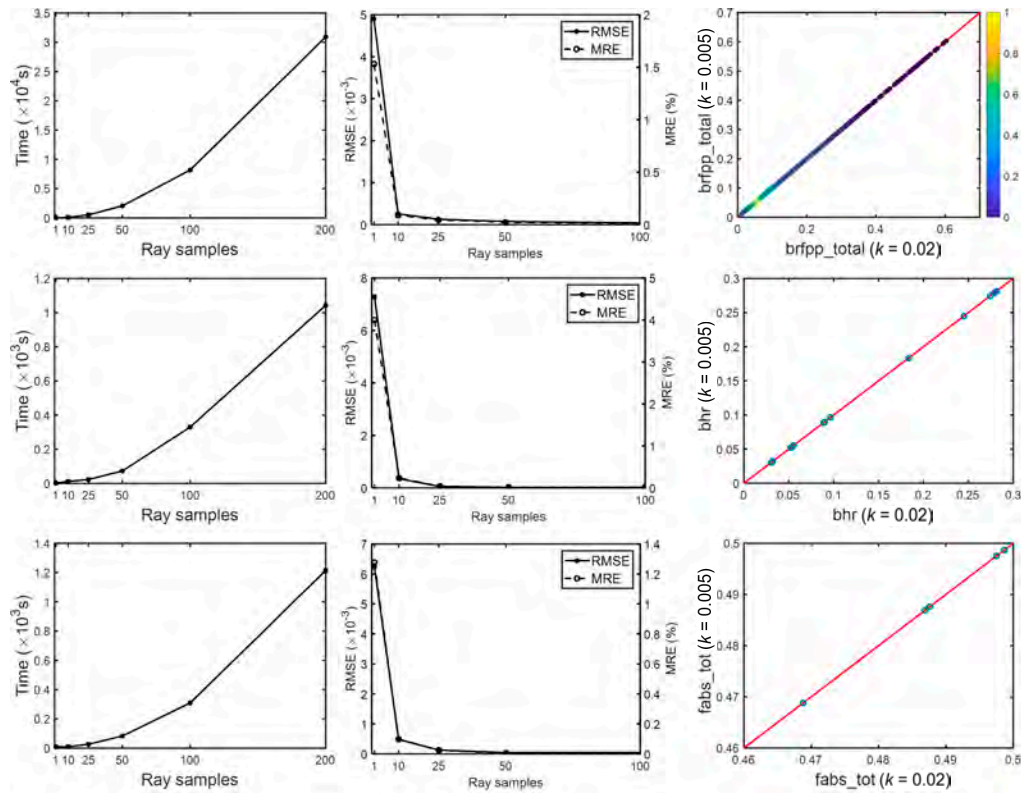
B HET51_WWO_TLS
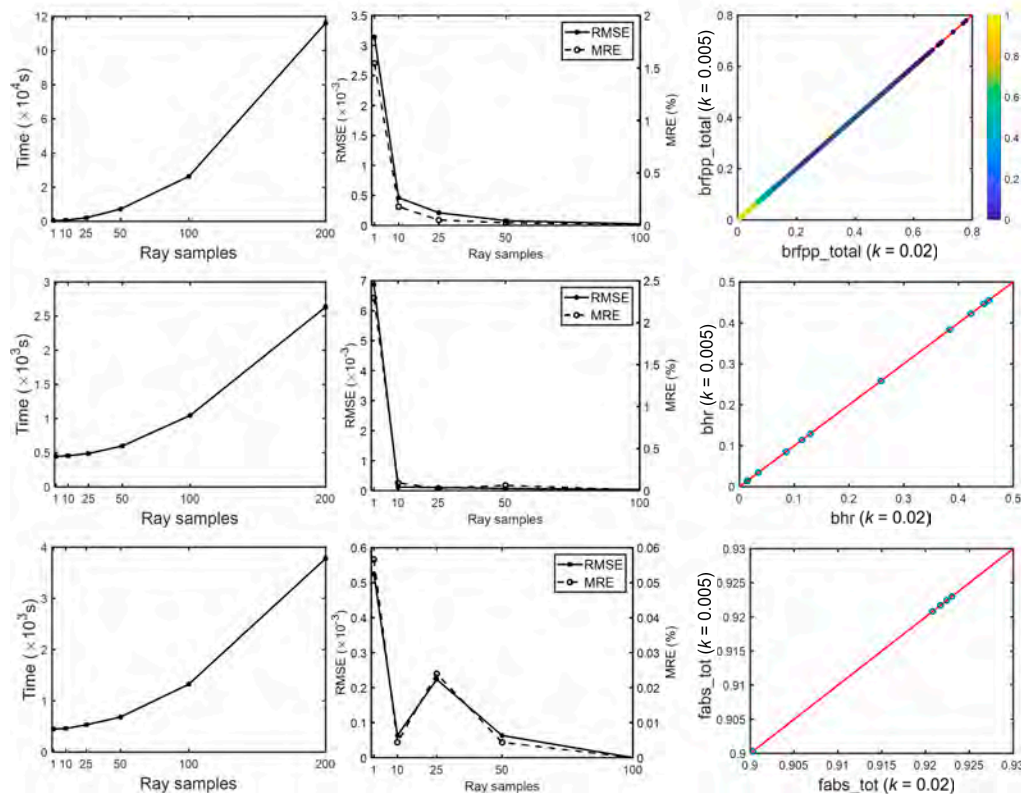
Fig. 19. The time consumption and errors of the *brfpp_total* (first row), *bhr* (second row), and *fabs_tot* (third row) simulations in 2 representative scenes. The sun geometries were fixed at z59a146 for HET16 (A) and z35a138 for HET51 (B), while all the bands and view geometries were considered. The first column displays the time for scene loading and simulating in total. The MREs and RMSEs in the second column were computed based on the simulation results for 200 ray samples. The color bars in the last column indicate the normalized density of the sample points, and the red lines are the 1:1 reference lines.

Discussion

RAMI-V limitations

As an intercomparison activity, RAMI-V struggles for the unity of all kinds of concepts and definitions opening to the participants. Indeed, most concepts and definitions have been described in detail on the RAMI-V webpages; however, some are confusing.

For those 3D basic geometries that have both lateral faces and base faces, whether the base faces need to be removed is unknown. In fact, these kinds of geometries are used in the structure of branches, stems, and grasses, which, to some extent, affect area computation of the wooden elements and grasses. For the scene HET16_SRF_UND, the area difference between before and after removal of the base faces reaches 811 m^2. Although the remaining base faces may alter scattering times, the simulation differences caused by it are basically negligible.

The foliage is transmissible in RAMI-V. Since the OBJ files are finally parsed into lots of triangles, the basic geometries used in the foliage cannot be identified as a whole in the transmission. For the conifer trees, the foliage is composed of ellipsoids; thus, the rays will transmit them twice. Because the transmittance is bound to OBJ triangles in LESS, if we directly input the foliage transmittance given by RAMI-V, the actual transmittance will decrease, which is bound to lead to simulation differences. The useful solution is to input the square root of the transmittance and set the reflectance of the inner surface to zero [60]. Of course, we think by default that the transmittance is bound to the whole ellipsoid due to practical spectral measurements, whereas in a simulation environment, the transmittance bound to triangles is also reasonable as long as it is stated in advance.

For traditional BRF simulations, the reference plane is clearly defined on the top of the canopy and covers the entire scene. RAMI-V continues to use this definition for a brand new measurement type *brf_sat*. However, the observed region of *brf_sat* for MSI is a central part of the entire scene, which is different from the observed regions of 2 other satellite instruments and traditional BRF simulations. As shown in Fig. 3, the reference plane defined on the top of the canopy will result in FOV difference in the case of *brf_sat* for MSI. RAMI-V did not seem to consider this problem. According to our understanding, the reference plane should be moved to the ground in order to maintain positional consistency. Once other RT models participating in RAMI-V continue to place the reference plane on the top of the canopy for *brf_sat* for MSI, the simulation results will become incomparable.

Since RAMI-V is an ongoing exercise, we cannot obtain the reference data from it; thus, we turned to the past RAMI phases. It is unfortunate that the description of the past RAMI phases is incomplete and confusing now. For example, on the page of the definition of *brfazim* in RAMI-IV, the illumination conditions do not come from RAMI-IV but from RAMI-V, which easily misleads the users. More seriously, the ROMC reference data lack simulations on actual scenes, which is why we used the ROMC reference data and Rayspread to respectively validate the abstract and actual scenes in the Validation with ROMC and Rayspread section. In addition, the ROMC reference data are not available in the digital form; therefore, if the users want to use it, they can only digitalize it from the figures.

Conclusion

This paper first reconstructs all the RAMI-V scenes in the standard OBJ format with simplified basic geometries and then employs different solvers provided by the LESS RT model to deal with various simulations demanded by RAMI-V. Benefiting from the "instance" technique and Python interface utilized by LESS, several usage problems (e.g., abstract structural description, nonuniform coordinate systems, and complex tree models) of RAMI scenes are successfully solved. The simulation results are fully evaluated by revealing some radiative phenomena, such as angle effects of BRF, energy conservation, and Beer's law. In addition, the parametric sensitivity analysis is performed, from which we can draw some conclusions: (a) The surface-area-unchanged simplification scheme is well validated by the ROMC reference data and Rayspread for the abstract and actual scenes. This scheme not only efficiently produces negligible simulation errors with less computational resource usage, but also ensures the consistency of the projected area, which matters with respect to those simulations concerned with structural parameters. (b) The optimal illumination resolution is suggested to be 0.02, which can implement fast and accurate simulation at the same time. Finally, this paper generates the standard OBJ models and reliable simulation results (all available on the website http://lessrt.org/3dscenes/), which can be used to validate other RT models and all kinds of retrieval algorithms in the future.

Acknowledgments

Data Availability

The reconstructed RAMI-V scenes in the standard OBJ format, organized in the form of the LESS project, are available on the website http://lessrt.org/3dscenes/.

Supplementary Materials

Table S1. Nadir orthographic images and digital camera photographs of representative abstract scenes and all the actual scenes simulated by LESS.

References

1. Qi J, Xie D, Yin T, Yan G, Gastellu-Etchegorry JP, Li L, Zhang W, Mu X, Norford LK. LESS: LargE-Scale remote sensing data and image simulation framework over heterogeneous 3D scenes. *Remote Sens Environ*. 2019;221:695–706.
2. Pinty B, Gobron N, Widlowski JL, Gerstl SAW, Verstraete MM, Antunes M, Bacour C, Gascon F, Gastellu JP, Goel N, et al.

Radiation transfer model intercomparison (RAMI) exercise. *J Geophys Res Atmos*. 2001;106:11937–11956.

3. Yang P, van der Tol C, Yin T, Verhoef W. The SPART model: A soil-plant-atmosphere radiative transfer model for satellite measurements in the solar spectrum. *Remote Sens Environ*. 2020;247:111870.

4. Jin D, Qi J, Huang H, Li L. Combining 3D radiative transfer model and convolutional neural network to accurately estimate Forest canopy cover from very high-resolution satellite images. *IEEE J Sel Top Appl Earth Obs Remote Sens*. 2021;14:10953–10963.

5. Verrelst J, Camps-Valls G, Muñoz-Marí J, Rivera JP, Veroustraete F, Clevers JGPW, Moreno J. Optical remote sensing and the retrieval of terrestrial vegetation bio-geophysical properties—A review. *ISPRS J Photogramm Remote Sens*. 2015;108:273–290.

6. Li L, Mu X, Soma M, Wan P, Qi J, Hu R, Zhang W, Tong Y, Yan G. An iterative-mode scan design of terrestrial laser scanning in forests for minimizing occlusion effects. *IEEE Trans Geosci Remote Sens*. 2021;59:3547–3566.

7. Yan G, Chu Q, Tong Y, Mu X, Qi J, Zhou Y, Liu Y, Wang T, Xie D, Zhang W, et al. An operational method for validating the downward shortwave radiation over rugged terrains. *IEEE Trans Geosci Remote Sens*. 2020;1–18.

8. Durrieu S, Cherchali S, Costeraste J, Mondin L, Debise H, Chazette P, Dauzat J, Gastellu-Etchegorry J-P, Baghdadi N, Pélissier R, Preliminary studies for a vegetation ladar/lidar space mission in France. Paper presented at: IEEE: Proceedings of the 2013 IEEE International Geoscience and Remote Sensing Symposium-IGARSS; 2013 Jul 21–26; Melbourne, VIC, Australia.

9. Verhoef W. Light scattering by leaf layers with application to canopy reflectance modeling: The SAIL model. *Remote Sens Environ*. 1984;16:125–141.

10. Li X, Strahler AH. Geometric-optical bidirectional reflectance modeling of the discrete crown vegetation canopy: Effect of crown shape and mutual shadowing. *IEEE Trans Geosci Remote Sens*. 1992;30:276–292.

11. Chen JM, Leblanc SG. A four-scale bidirectional reflectance model based on canopy architecture. *IEEE Trans Geosci Remote Sens*. 1997;35:1316–1337.

12. Zeng Y, Li J, Liu Q, Huete AR, Yin G, Xu B, Fan W, Zhao J, Yan K, Mu X. A radiative transfer model for heterogeneous agro-forestry scenarios. *IEEE Trans Geosci Remote Sens*. 2016;54:4613–4628.

13. Qin W, Gerstl SA. 3-D scene modeling of semidesert vegetation cover and its radiation regime. *Remote Sens Environ*. 2000;74:145–162.

14. Huang H, Qin W, Liu Q. RAPID: A Radiosity applicable to porous IndiviDual objects for directional reflectance over complex vegetated scenes. *Remote Sens Environ*. 2013;132:221–237.

15. Wang Y, Kallel A, Yang X, Regaieg O, Lauret N, Guilleux J, Chavanon E, Gastellu-Etchegorry JP. DART-Lux: An unbiased and rapid Monte Carlo radiative transfer method for simulating remote sensing images. *Remote Sens Environ*. 2022;274:112973.

16. Widlowski JL, Lavergne T, Pinty B, Verstraete M, Gobron N. Rayspread: A virtual laboratory for rapid BRF simulations over 3-D plant canopies. In Graziani F, editor. *Computational Methods in Transport. Lecture Notes in Computational Science and Engineering*. Berlin, Heidelberg: Springer; 2006. vol. 48, pp. 211–231.

17. Kobayashi H, Iwabuchi H. A coupled 1-D atmosphere and 3-D canopy radiative transfer model for canopy reflectance, light environment, and photosynthesis simulation in a heterogeneous landscape. *Remote Sens Environ*. 2008;112:173–185.

18. Thompson RL, Goel NS. Two models for rapidly calculating bidirectional reflectance of complex vegetation scenes: Photon spread (PS) model and statistical photon spread (SPS) model. *Remote Sens Rev*. 1998;16:157–207.

19. Goodenough AA, Brown SD. DIRSIG 5: Core design and implementation. In: *Algorithms and technologies for multispectral, hyperspectral, and ultraspectral imagery XVIII*. International Society for Optics and Photonics; 2012. p. 124–132.

20. Li W, Guo Q, Tao S, Su Y. VBRT: A novel voxel-based radiative transfer model for heterogeneous three-dimensional forest scenes. *Remote Sens Environ*. 2018;206:318–335.

21. Yan K, Zhang Y, Tong Y, Zeng Y, Pu J, Gao S, Li L, Mu X, Yan G, Rautiainen M, et al. Modeling the radiation regime of a discontinuous canopy based on the stochastic radiative transport theory: Modification, evaluation and validation. *Remote Sens Environ*. 2021;267:112728.

22. Bian Z, Wu S, Roujean J, Cao B, Li H, Yin G, du Y, Xiao Q, Liu Q. A TIR forest reflectance and transmittance (FRT) model for directional temperatures with structural and thermal stratification. *Remote Sens Environ*. 2022;268:112749.

23. Song W, Mu X, McVicar TR, Knyazikhin Y, Liu X, Wang L, Niu Z, Yan G. Global quasi-daily fractional vegetation cover estimated from the DSCOVR EPIC directional hotspot dataset. *Remote Sens Environ*. 2022;269:112835.

24. Malenovský Z, Homolová L, Zurita-Milla R, Lukeš P, Kaplan V, Hanuš J, Gastellu-Etchegorry JP, Schaepman ME. Retrieval of spruce leaf chlorophyll content from airborne image data using continuum removal and radiative transfer. *Remote Sens Environ*. 2013;131:85–102.

25. Prusinkiewicz P, Lindenmayer A. *The algorithmic beauty of plants;* New York: Springer Science & Business Media; 2012.

26. Liu Z, Wu K, Guo J, Wang Y, Deussen O, Cheng Z. Single image tree reconstruction via adversarial network. *Graph Model*. 2021;117:101115.

27. Calders K, Origo N, Burt A, Disney M, Nightingale J, Raumonen P, Åkerblom M, Malhi Y, Lewis P. Realistic forest stand reconstruction from terrestrial LiDAR for radiative transfer modelling. *Remote Sens*. 2018;10:933.

28. Qi J, Xie D, Yan G, Gastellu-Etchegorry JP. Simulating spectral images with less model through a voxel-based parameterization of airborne lidar data. Paper presented at: IEEE: Proceedings of the IGARSS 2019-2019 IEEE International Geoscience and Remote Sensing Symposium; 2019 Jul 28–Aug 2; Yokohama, Japan.

29. Qi J, Xie D, Jiang J, Huang H. 3D radiative transfer modeling of structurally complex forest canopies through a lightweight boundary-based description of leaf clusters. *Remote Sens Environ*. 2022;283:113301.

30. Zhao F, Li Z, Verhoef W, Fan C, Luan H, Yin T, Zhang J, Liu Z, Tong C, Bao Y. Simulation of solar-induced chlorophyll fluorescence by modeling radiative coupling between vegetation and atmosphere with WPS. *Remote Sens Environ*. 2022;277:113075.

31. Liu C, Calders K, Meunier F, Gastellu-Etchegorry JP, Nightingale J, Disney M, Origo N, Woodgate W, Verbeeck H. Implications of 3D forest stand reconstruction methods for

radiative transfer modeling: A case study in the temperate deciduous forest. *J Geophys Res-Atmos*. 2022;127.

32. Pinty B, Widlowski J-L, Taberner M, Gobron N, Verstraete MM, Disney M, Gascon F, Gastellu J-P, Jiang L, Kuusk A, et al. Radiation Transfer Model Intercomparison (RAMI) exercise: Results from the second phase. *J Geophys Res Atmos*. 2004;109(D6):D6210.

33. Widlowski JL, Taberner M, Pinty B, Bruniquel-Pinel V, Disney M, Fernandes R, Gastellu-Etchegorry JP, Gobron N, Kuusk A, Lavergne T, et al. Third Radiation Transfer Model Intercomparison (RAMI) exercise: Documenting progress in canopy reflectance models. *J Geophys Res*. 2007;112.

34. Widlowski JL, Pinty B, Lopatka M, Atzberger C, Buzica D, Chelle M, Disney M, Gastellu-Etchegorry JP, Gerboles M, Gobron N, et al. The fourth radiation transfer model intercomparison (RAMI-IV): Proficiency testing of canopy reflectance models with ISO-13528. *J Geophys Res Atmos*. 2013;118:6869–6890.

35. Widlowski J, Mio C, Disney M, Adams J, Andredakis I, Atzberger C, Brennan J, Busetto L, Chelle M, Ceccherini G, et al. The fourth phase of the radiative transfer model intercomparison (RAMI) exercise: Actual canopy scenarios and conformity testing. *Remote Sens Environ*. 2015;169:418–437.

36. Li W, Mu X. Using fractal dimension to correct clumping effect in leaf area index measurement by digital cover photography. *Agric For Meteorol*. 2021;311:108695.

37. Grau E, Durrieu S, Fournier R, Gastellu-Etchegorry JP, Yin T. Estimation of 3D vegetation density with Terrestrial Laser Scanning data using voxels. A sensitivity analysis of influencing parameters. *Remote Sens Environ*. 2017;191:373–388.

38. Hu R, Yan G, Mu X, Luo J. Indirect measurement of leaf area index on the basis of path length distribution. *Remote Sens Environ*. 2014;155:239–247.

39. Gastellu-Etchegorry J, Yin T, Lauret N, Cajgfinger T, Gregoire T, Grau E, Feret JB, Lopes M, Guilleux J, Dedieu G, et al. Discrete anisotropic radiative transfer (DART 5) for modeling airborne and satellite spectroradiometer and LIDAR acquisitions of natural and urban landscapes. *Remote Sens*. 2015;7:1667–1701.

40. Yan G, Jiang H, Luo J, Mu X, Li F, Qi J, Hu R, Xie D, Zhou G. Quantitative evaluation of leaf inclination angle distribution on leaf area index retrieval of coniferous canopies. *J Remote Sens*. 2021;2021:2708904.

41. Pisek J, Lang M, Nilson T, Korhonen L, Karu H. Comparison of methods for measuring gap size distribution and canopy nonrandomness at Järvselja RAMI (RAdiation transfer model Intercomparison) test sites. *Agric For Meteorol*. 2011;151:365–377.

42. Calders K, Origo N, Disney M, Nightingale J, Woodgate W, Armston J, Lewis P. Variability and bias in active and passive ground-based measurements of effective plant, wood and leaf area index. *Agric For Meteorol*. 2018;252:231–240.

43. Widlowski JL, Pinty B, Lavergne T, Verstraete MM, Gobron N. Using 1-D models to interpret the reflectance anisotropy of 3-D canopy targets: Issues and caveats. *IEEE Trans Geosci Remote Sens*. 2005;43:2008–2017.

44. Lintermann B, Deussen O. Interactive modeling of plants. *IEEE Comput Graph Appl*. 1999;19:56–65.

45. J. Weber, J. Penn. Creation and rendering of realistic trees. Paper presented at: Proceedings of the 22nd Annual Conference on Computer Graphics & Interactive Techniques; 1995 September.

46. Disney MI, Lewis P, Gomez-Dans J, Roy D, Wooster MJ, Lajas D. 3D radiative transfer modelling of fire impacts on a two-layer savanna system. *Remote Sens Environ*. 2011;115:1866–1881.

47. Raumonen P, Kaasalainen M, Åkerblom M, Kaasalainen S, Kaartinen H, Vastaranta M, Holopainen M, Disney M, Lewis P. Fast automatic precision tree models from terrestrial laser scanner data. *Remote Sens*. 2013;5:491–520.

48. Akerblom M, Raumonen P, Casella E, Disney MI, Danson FM, Gaulton R, Schofield LA, Kaasalainen M. Non-intersecting leaf insertion algorithm for tree structure models. *Interface Focus*. 2018;8:20170045.

49. Vouk V. Projected area of convex bodies. *Nature*. 1948;162:330–331.

50. Rahman H, Verstraete MM, Pinty B. Coupled surface-atmosphere reflectance (CSAR) model: 1. Model description and inversion on synthetic data. *J Geophys Res Atmos*. 1993;98:20779–20789.

51. Widlowski JL, Robustelli M, Disney M, Gastellu-Etchegorry JP, Lavergne T, Lewis P, North PRJ, Pinty B, Thompson R, Verstraete MM. The RAMI on-line model checker (ROMC): A web-based benchmarking facility for canopy reflectance models. *Remote Sens Environ*. 2008;112:1144–1150.

52. Jiao Z, Ren H, Mu X, Zhao J, Wang T, Dong J. Evaluation of four sky view factor algorithms using digital surface and elevation model data. *Earth Space Sci*. 2019;6:222–237.

53. Li X, Huang H, Shabanov NV, Chen L, Yan K, Shi J. Extending the stochastic radiative transfer theory to simulate BRF over forests with heterogeneous distribution of damaged foliage inside of tree crowns. *Remote Sens Environ*. 2020;250:112040.

54. Pu J, Yan K, Zhou G, Lei Y, Zhu Y, Guo D, Li H, Xu L, Knyazikhin Y, Myneni RB. Evaluation of the MODIS LAI/FPAR algorithm based on 3D-RTM simulations: A case study of grassland. *Remote Sens*. 2020;12:3391.

55. Kajiya JT. The rendering equation. *ACM Comput Graph*. 1986;20(4):143–150.

56. De Wit CT, Photosynthesis of leaf canopies. In: *Agricultural research report no. 663*. Wageningen (The Netherlands): Center for Agricultural Publication and Documentation; 1965. p. 1–57.

57. Ross J. *The radiation regime and architecture of plant stands*. The Hague (The Netherlands): Springer; 1981.

58. Tang S, Chen JM, Zhu Q, Li X, Chen M, Sun R, Zhou Y, Deng F, Xie D. LAI inversion algorithm based on directional reflectance kernels. *J Environ Manag*. 2007;85:638–648.

59. Zhou X, Zhu Q, Tang S, Chen X, Wu M. Interception of PAR and relationship between FPAR and LAI in summer maize canopy. Paper presented at: IEEE: Proceedings of the IEEE International Geoscience and Remote Sensing Symposium. 2002 Jun 24–28; Toronto, Ontario, Canada.

60. Qi J, Xie D, Guo D, Yan G. A large-scale emulation system for realistic three-dimensional (3-D) forest simulation. *IEEE J Sel Top Appl Earth Obs Remote Sens*. 2017;10:4834–4843.